Punch Penetration Tests – The Better Input Parameter for TBM Performance Prediction?

Hartmut Erben

Table of contents

1. Introduction

1.1 Objectives, tasks and definition of the problem

Performance prediction for tunnel boring machines (TBM) is a crucial topic for the construction industry as it is one of the key factors to determine construction time. For such performance prediction models, the uniaxial compressive strength of rock is today used as a key input parameter. The failure mechanism for compressive strength is, however, not very close to the process of mechanical rock breakage in TBM tunneling from a fracture mechanics point of view.

A rock property that is very close to real mechanical rock breakage and affects boreability very much is brittleness, because rock cutting efficiency improves with increased brittleness. There is no well-established standard test for measuring rock brittleness in a laboratory test. However, the Colorado School of Mines developed the so called “Punch Penetration Test” which is considered to be one of the most applicable tests for the assessment of rock brittleness.

One of the goals of the research is to investigate the relationship between the results obtained from Punch Penetration Tests and intact rock properties from linear cutting tests (that were carried out at the Earth Mechanics Institute (EMI) of the Colorado School of Mines) and geotechnical standard laboratory tests such as Uniaxial Compressive Strength (UCS), Brazilian Tensile Strength (BTS), mineralogical and petrographical investigations. In order to find mathematical relations between these tests, statistical analysis governed by a rock mechanical interpretation will be carried out.

There is no standard parameter derived from punch penetration tests. Therefore another important topic of this study will be the search for a key parameter or characteristic value for the application of Punch Penetration Test results.

The research is done on rock samples from the following eastern alpine lithologies: Brixen Granite, Granite Gneiss, Imberg Sandstone, Augen Gneiss and a Calcareous Mica Schist which have not been tested with punch penetration tests before. The knowledge about the excavatability and brittleness of these lithologies is very important for many European tunneling projects. For example one of the biggest upcoming European tunneling projects will be the Brenner Base Tunnel with a length of about 55 km (34.2 miles) with approximately XX km driven through Brixen Granite.

The results of the research will help to determine the most appropriate testing procedure for TBM performance prediction and give an insight into what happens inside the rock sample during the loading procedure of the Punch Penetration Test.

1.2 PPT / Indentation tests

1.2.1 Brittleness

Brittleness is one of the most popular research topics in rock mechanics nowadays *[4,5,7,13,26]*, but until now there is no standardized way to measure and quantify rock brittleness. Although many scientists have been working on a single definition of brittleness, no common definition is available yet.

The positive effect of increasing brittleness on rock cutting efficiency is not yet fully understood.

"However, it may be stated that with higher brittleness the following facts are observed:

- *Low values of elongation;*
- *Fracture failure;*
- *Formation of fines;*
- *Higher ratio of compressive to tensile strength;*
- *Higher resilience;*
- *Higher angle of internal friction;*

Formation of cracks in indentation;" *[1]*

This means that that the more brittle a rock is, the less deformation it can take. In most cases this leads to the conclusion that for the same amount of debris less energy is consumed.

Many engineers put a lot of effort into describing rock brittleness, because it is a rock property that is very close to the real mechanical rock breakage and affects boreability very much.

"The property of brittleness can be considered as the inverse of ductility. The degree of brittleness is usually reflected in low values of per cent elongation or reduction of area or, if true strain values are used, in low values of ε_p *or* $\varepsilon_?$*."* *[2]*

"Brittle fracture is defined as fracture that exhibits no or little permanent (plastic) deformation." *[3]*

Bieniawski (1967) postulated a mechanism of brittle rock fracture in multiaxial compression:

1. Closing of cracks
    I. Crack closure
2. Linear elastic deformation
    II. Fracture initiation
3. Stable fracture propagation
    III. Critical energy release
4. Unstable fracture propagation
    IV. Strength failure (maximum stress) – onset of forking
5. Forking and coalescence of cracks
        V. Rupture (maximum deformation) *[3]*

Over years rock brittleness was obtained indirectly as a function of rock strength.

In engineering practices there are three empirical concepts for obtaining brittleness,

$$B_1 = \frac{\sigma_C}{\sigma_T}$$

$$B_2 = \frac{\sigma_C - \sigma_T}{\sigma_C + \sigma_T}$$

$$B_3 = \frac{\sigma_C * \sigma_T}{2}$$

where, B_1, B_2 and B_3 are the obtained brittleness values, σ_c is the uniaxial compressive strength (MPa) and σ_T is the tensile strength of rock (MPa). *[4]*

In recent years the punch penetration test, which was developed in the 1970's, has been used to measure brittleness directly as an index value. The inventor of this new brittleness index (BI_m) is Saffet Yagiz, who was working on several projects at the Earth

Mechanics Institute of the Colorado School of Mines in order to utilize the punch penetration test. [5]

Yagiz used the the maximum applied force (F_{max}, kN) on the specimen and the corresponding penetration (P, mm) and named the ratio rock brittleness index (BI_m, kN/mm).

$$BI_m = \frac{F_{max}}{P}$$

The results of Yagiz research is a new formula to calculate/predict the brittleness index (BI_p) as a function of compressive strength (σ_c), tensile strength (σ_T) and density of the rock (ρ), if the expensive and uncommon laboratory equipment for the punch penetration test is not available.

$$BI_p = 0{,}198 * \sigma_c - 2{,}174 * \sigma_t + 0{,}913 * \rho - 3{,}807$$

1.2.2 Development of the Punch Penetration Test

The Punch Penetration Test (PPT) was developed in the late 1960s out of the desire to provide a direct laboratory testing method for estimating the normal loads on disc cutters during the mechanical excavation of shafts with raise boring technology and tunnels.

Among numerous companies which are using the PPT nowadays, there are two outstanding manufacturers that did a lot of the early development. Those two companies were Robbins Company and the Raise Drill Division of Ingersoll Rand, which was bought by Robbins in 1979.

The indirect tests that are used for TBM performance prediction, such as the Uniaxial Compressive Strength (UCS) and the Brazilian Tensile Strength (BTS), measure rock strength parameters and differ therefore very much from the Punch Penetration Test, which is a direct test to measure the load and penetration under a cutter or indenter.

As a direct test the PPT belongs in the same category of direct laboratory tests as the rotary cutting test and the linear cutting test, which are both methods for determining normal loads under cutting tools during excavation.

The main advantages of the PPT are the small size samples, which can easily be gained out of exploratory drilling cores and the cheap and simple testing procedure compared to the two full scale tests. The linear and the rotary cutting test both need

large rock blocks, which will never be available in the early stages of a project, where it would be necessary to estimate TBM performance and costs.

The punch penetration test that was originally used by Robbins consisted of a hydraulic ram which pressed a button indenter into a saw cut surface of a rock core. The indenter was conical in shape and made out of tungsten-carbide to prevent abrasive wear. This indenter had a 120° included angle with a 3,175 mm tip radius.

The sample was confined by Hydrostone (a high-strength Hydrocal plaster) within a steel cylinder while testing.

During a test displacement and load on the indenter were monitored.

The main modifications of the PPT over the years affected the way the displacement of the indenter is controlled and the way data is collected and monitored. The loading capacity and stiffness of the apparatus were increased as well as the maximum achievable depth of penetration. Another important change was the modification of the loading procedure from periodic loading to a non-cyclical continuous loading rate.

A lot of testing was also carried out with different shapes of the indenters, ranging from sharp wedge indenters to sections of disc cutters to spherical tipped indenters. Most of those tests were done to find out how the shape affects the force-penetration relationship and how the failure mode changes. *[6]*

Until today there is no guideline or standardized procedure how to perform the PPT. This leads to many different settings as far as the shape of the indenter, the size of the samples and the loading rate is concerned.

R. Gertsch for example compared the results of PPT carried out with rock cores of 54 mm diameter with results obtained from PPT on large blocks with an edge length of 270 mm. The outcome of his research was that the PPT carried out on the blocks lead to a slightly more accurate prediction of the specific energy, the specific penetration and the cutting forces of disc cutter tests performed on the same lithologies. *[7]*

These results do not really surprise, because the confinement of the block is a lot better than the confinement the Hydrostone can provide. Furthermore block indentation tests miss the point of the PPT, which was designed to provide an easy and cheap direct method for estimating loads on disc cutters during the mechanical excavation of rock and the test just stays cheap as long as the sample sizes are small.

Fracture analysis of rock under disc cutters / indenters

Studying the indentation process of an indenter has led to great knowledge on the failure mechanisms of rock under both indenters or bits and disc cutters. The shape of an indenter reaches from hemispherical, conical to sharp wedge shapes, whereas a disc cutter is a steel ring.

There are several zones evolving during an indentation process:

Directly under the disc a primary crushed zone of highly fractured and inelastically deformed rock forms *[8]*, which is under a quasi-hydrostatic state of stress. If the load is high enough to produce a shearing stress greater than the shearing strength of the material, a major fracture occurs in axial direction under the indenter. Beneath the primary zone a secondary crushed zone forms, caused by the load transfer through the primary zone. The size of the crushed zone depends on the confinement of the surrounding material and the secondary crushed zone is generally larger and deeper than the primary zone.

Outside the crushed zone tension cracks emerge in radial direction and this zone is referred to as the cracked zone. If these radial cracks reach the surface or meet other cracks caused by adjacent discs, large chips erupt from the surface.

The aim of every cutting process in TBM tunneling is that chips form as soon as possible, because it is the most efficient and energy saving way to excavate hard rock.

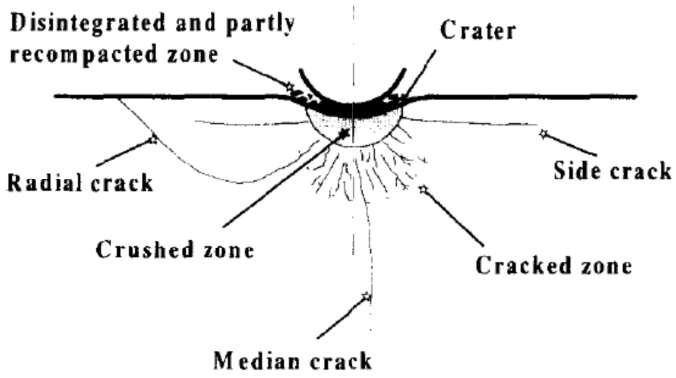

Figure 1: General picture of fracture systems in rock under indentation (Lindqvist et al., 1994) ***[9]***

Another thing that needs to be mentioned is that type, size and direction of fractures is influenced by many different material properties such as grain size, cleavage planes, schistosity and grain ponding. A pore or any nearby void can deflect cracks from their preferred path. *[10]*

In his Dissertation Gertsch made a lot of damage assessment for both, the interior and the surface damage of his block and core indentation tests. To investigate the interior damage the samples were sawn apart along the axis of indentation. *[7]*

One of his main observations was that the blocks, which generally better represent the semi-infinite surface area of the tunnel face, exhibit a shallower failure mechanism than the cores. The usually characteristic median crack only formed few times in the block indentation tests and the internal damage does not extend much further than the bottom of the indentation crater. The core samples showed deep median cracks emerging from the indenter vertically into the sample, several cracks radiating outward from the crater and the secondary crushed zone extended a few times the penetration depth into the rock.

H.Y. Liu et al were able to show the same results by simulating the indentation process with numerical simulation. *[11]*

This is easy to explain because the confinement of the cores embedded in Hydrostone and a steel ring is less stiff than the confinement of the indented area in the block tests, which is solid, homogenous rock with no interruption.

Nowadays computers have reached a power level where many indentation tests can be simulated with numerical programs. The three main numerical methods, the finite element method (FEM), the boundary element method (BEM) and the discrete element method (DEM), coupled with fracture models, are used to calculate stress fields and simulate the fracture under an indenter by many researchers. *[11]*

The theoretical solution for contact problems and classical contact mechanics is always associated with Heinrich Hertz. He analyzed the elastic contact between two curved bodies in 1881. Later on he described the conical shaped crack that runs around the contact circle between the two bodies and found that the crack spreads into one of the bodies at critical loading. *[11]*

Hertz offered the classical solutions for non-adhesive elastic contact between a sphere and an elastic half space as well as the contact between a rigid cylinder and an elastic half space.

Solutions for the point contact of a concentrated normal load on a three dimensional half-space were found by Boussinesq in 1885 and are known as the Boussinesq field.

The pictures show the difference in the stress trajectories for the Hertzian field as well as the Boussinesq field.

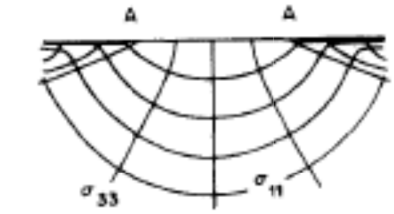

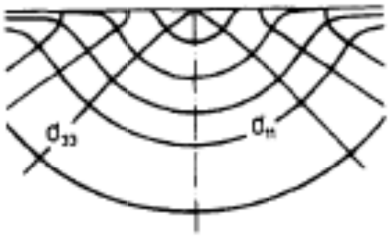

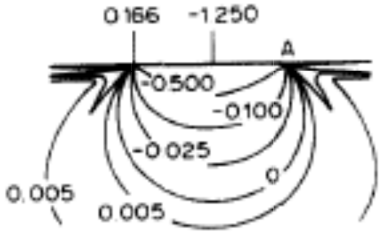

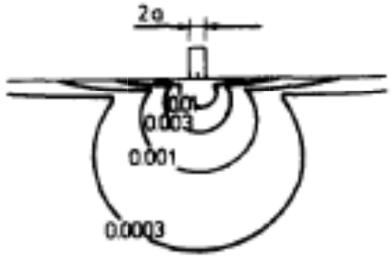

ories σ11 zian otes and

tories of σ11 n) in 20. 2a After

1.3 Performance Prediction

1.3.1 Input parameters for the prediction models

Performance prediction models for tunnel boring machines are today more important, than they have ever been before, because construction time is one of the most crucial cost drivers for each tunneling project. Consequently the accurate estimation of the construction schedule has become a thing of high importance to estimate construction cost.

The accuracy of TBM performance prediction models relies undoubtably on the quality and reliability of the input parameters. These parameters are derived from from geotechnical explorations and vary from one prediction model to the other. As there are numerous performance prediction models for different mining and tunneling applications, it is important to find the most applicable model for the current project.

Not only the selection of the suitable prediction model, but also the choice of the proper tunnel boring machine depends on the site investigation because TBMs are in most cases manufactured for one specific site. Geotechnical exploration is of great importance for TBM-projects and rock engineering projects in general and should be carried out carefully to obtain the basis for a successful project.

These facts lead to the conclusion that the performance of a TBM depends on machine specifications, intact rock properties and rock mass characterization.

The machine specifications, such as diameter, thrust, power, torque and cutting geometry (geometry of the cutter discs, spacing between two adjacent discs, size of the muck buckets…) are consistent and easy to get and should be quantified carefully, but as soon as it comes to the properties of the rock, each prediction model uses its own input parameters.

Especially one rock parameter, namely brittleness, is currently not really considered in these models. There are efforts to include a brittleness factor in the Colorado School of Mines model as well as in the Norges teknisk-naturvitenskapelige universitet (NTNU) model, but the improvements have not really found their way to the construction site.

The result of a prediction model is in most cases, despite of the varying input parameters, an estimated rate of penetration (ROP) in millimeter per revolution (mm/rev). This is the excavated distance after one revolution of the cutterhead.

The prediction of the ROP does not necessarily make it easy for the construction company to estimate construction time because in TBM tunneling the processes of excavation and support can be very complex. This means, that there are more factors to consider to assume construction time.

The common methods to calculate daily advance rates are rather simple. The following formulas explain how the daily advance rates are calculated traditionally:

$$I_n = \frac{p * n_B * 60}{1000}$$

I_n net penetration [m/h]

P penetration [mm/rev]

n_B cutterhead speed [rev/min]

$$Q = u * I_n * t_{VS}$$

Q advance rate [m/d]

u utilisation degree [%]

t_{VS} daily working time [h/d] *[12]*

Subsequently three different prediction models will be introduced.

1.3.2 Colorado School of Mines (CSM) model

The Colorado School of Mines (CSM) model was developed by the Earth Mechanics Institute (EMI) at the Colorado School of Mines as a model for TBM performance prediction over the last 35 years.

Ozdemir published the initial formulation of the CSM model in the late 1970s as a result of the research done at the EMI. In the following years the CSM model was consequently modified and improved to keep up with the development in the tunneling industry (Rostami 1997: change in the shape of disc cutters from V-discs to constant cross-section discs; transferred the model into dimensional stable equations) and is still in progression nowadays. *[13, 14]*

The CSM model rests upon theoretical and empirical knowledge and experience. The empirical data comes from full-scale linear cutting tests and the collection of extensive field data.

It is based on various laboratory tests that measure intact rock properties such as the Uniaxial Compressive Strength (UCS) and the Brazilian Tensile Strength (BTS). In addition it is supported by linear cutting tests and sometimes Punch Penetration Tests.

The disadvantage of intact rock properties is that the results reflect those worst case rock mass properties, which do not consider any fractures and bedding planes, by underestimating the ROP. On the other hand it gives more conservative values, so that construction time will not be underestimated.

Input parameters for the CSM model:

Rock Properties	***Symbol***	***Unit***
Uniaxial Compressive Strength UCS	σ_c	MPa
Brazilian Tensile Strength BTS	σ_t	MPa
Machine parameters	***Symbol***	***Unit***
TBM cutterhead diameter	D_c	m
Cutter radius	R	mm
Spacing	S	mm
Disc tip width	T	mm
Number of disc cutters	n_c	-
Rotational speed	n	min^{-1}

The calculation to get the desired penetration which is possible under the circumstances given by the input parameters, takes place iteratively. This means you need to guess a penetration first and then go into the equations to see if your machine parameters, in this case the maximum cutting force, power and torque are not exceeded. If the penetration is still below the maximum values, it can be increased step by step until it hits the maximum of one of those parameters.

In case a certain penetration is given you can easily calculate the demanded machine parameters and design the TBM in order to fit the needs of this certain site.

$$\varphi = \operatorname{acos}\left(\frac{R-p}{R}\right)$$

$$P^* = 2{,}12 * \sqrt[3]{\frac{\sigma_c^2 * \sigma_t * S}{\varphi * \sqrt{R * T}}}$$

$$F = P^* * R * \varphi * T$$

$$M = n_c * 0{,}6 * \frac{D_c}{2} * F * sin\frac{\varphi}{2}$$

$$P = \frac{\pi}{30} * n * M$$

p	Penetration (mm)
φ	Angle of the contact area (rad)
P^*	Averaging stress in the contact area (MPa) / Uniform pressure
F	Cutting force (kN)
M	Torque (kNm)
P	Power requirement (MW)

[14]

1.3.3 NTNU model

The NTNU model is an empirical model and mainly based on TBM field data from tunneling projects with an overall length of 250 km. Regression analyses have been carried out to find a correlation between machine parameters, rock properties, ground conditions and the penetration rate.

Development of this model started in the mid 1970s, and was first published in 1976. *[15]*

The advantage of the NTNU model over the CSM model is that it considers rock mass properties and the excavation system in their entire complexity and is therefore widely accepted and used in the industry.

On the other hand is the forecasting ability of empirical models limited, because they rely on old data and this causes problems if a type of rock is encountered, that no TBM with certain specifications has excavated before.

Input parameters for the NTNU model:

Rock Properties	***Symbol***	***Unit***	
Fracturing: frequency and orientation	$k_{s\text{-}tot}$	-	
Drilling rate index DRI	k_{DRI}	-	
Porosity	k_{por}	-	
Machine parameters	***Symbol***	***Unit***	
TBM cutterhead diameter	D_c	m	
Cutter diameter	d	mm	
Cutter spacing	S	mm	
Cutter thrust	M_B	kN	
Installed cutterhead power	P	MW	
Number of disc cutters	n_c	-	
Rotational speed	n	min^{-1}	*[16]*

The NTNU model is a penetration rate model based on penetration curves which are derived from penetration tests performed by TBMs during different tunneling projects. The basic features of a penetration curve are the critical cutter thrust M_1 and the penetration coefficient b.

As a result, the basic penetration rate i_0 is calculated out of the following three parameters:

$$i_0 = \left(\frac{M_{equ}}{M_1}\right)^b$$

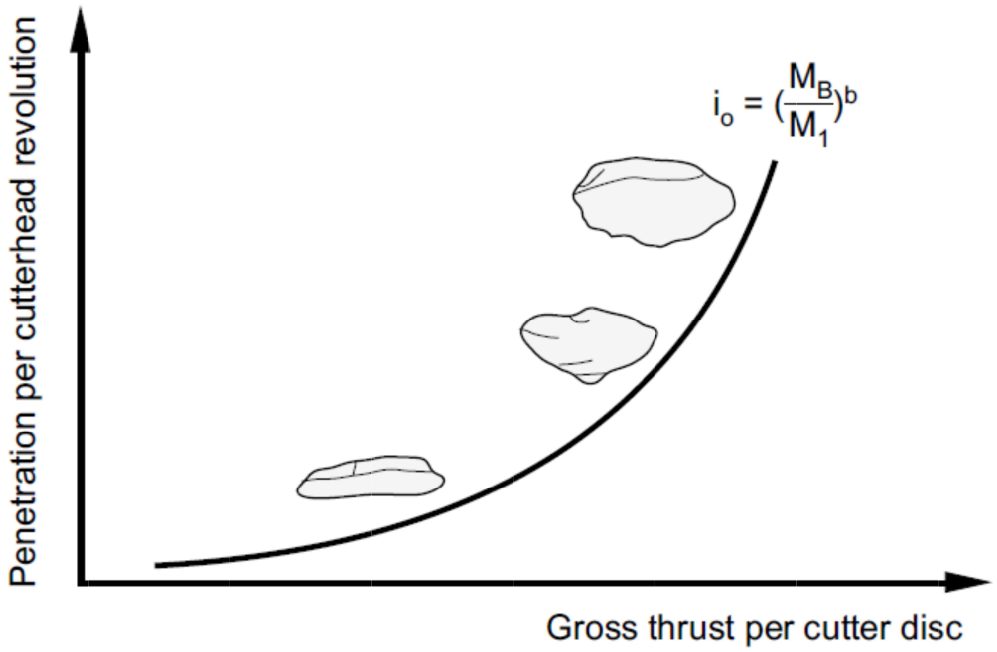

Figure 4: Penetration per cutterhead revolution based on thrust per cutter disc *[16]*

These three parameters (equivalent cutter thrust, critical cutter thrust and penetration coefficient) are determined by the consideration of different correction factors which are provided in tables and diagrams.

The influence of the machine parameters is aggregated in the equivalent cutter thrust M_{equ}:

$$M_{equ} = M_B * k_d * k_a$$

On the other hand the equivalent fracturing factor k_{equ} aggregates the influence of the rock mass properties. k_{equ} is necessary for the determination of the critical cutter thrust M_1 and the penetration coefficient b.

$$k_{equ} = k_{s-tot} * k_{DRI} * k_{por}$$

If there is more than one set of weakness planes in the model, the total fracturing factor $k_{s\text{-}tot}$ has to be calculated. k_s considers the average spacing between planes of weakness and the angle between the tunnel axis and the planes of weakness.

$$k_{s-tot} = \sum_{i=1}^{n} k_{si} - (n-1) * 0{,}36$$

[16]

i_0 Penetration per cutterhead revolution (mm/rev) / Basic penetration rate

M_{equ}	Equivalent cutter thrust (kN/disc)
M_1	Critical cutter thrust (to achieve a penetration of 1 mm/rev) (kN/disc)
b	Penetration coefficient (-)
M_B	Mean cutter thrust (kN/disc)
k_d	Correction factor for disc diameter (-)
k_a	Correction factor for mean spacing (-)
k_{equ}	Equivalent fracturing factor (-)
$k_{s\text{-}tot}$	Total fracturing factor (-) (considers all sets of weakness planes)
k_{DRI}	Factor for the drilling rate index DRI (-)
k_{por}	Porosity factor (-)
k_{si}	Fracturing factor for set number i
n	Number of fracturing sets

Compared to the CSM model, the NTNU model incorporates a very important aspect of mechanical excavation – the degree of fracturing in the rock mass. This crushing of the rock through its geological history before it comes to the first contact with a TBM saves a lot of excavation energy and construction time.

1.4 Sample description

Six different rock types were considered for this investigation. Three of them, Augen Gneiss, Calcareous Mica Schist and Granite Gneiss were tested under different loading directions to find out how the angle between loading direction and foliation affects the excavation. For the Schist Gneiss only samples with an oblique foliation were available. Brixen Granite and Imberg sandstone are isotropic .

Attention to the direction of the foliation was only paid for the linear cutting tests and the punch penetration tests, not for the geotechnical standard tests.

The laboratory testing program with the PPT comprised 53 rock cores, 18 samples for UCS and 18 samples for BTS.

	Lithology	**Direction to Foliation**		**Type**	**Number of Samples**		
1	**Augen Gneiss**	3 Directions	Normal	1	4		
			Parallel	2	4		
			Oblique	3	4		
2	**Calcareous Mica Schist**	3 Directions	Normal	4	5		
			Parallel	5	4		
			Oblique	6	4		
3	**Granite Gneiss**	2 Directions	Normal	7	5		
			Parallel	8	4		
4	**Brixen Granite**	1 Direction	Oblique	10	4		
5	**Imberg Sandstone**	1 Direction	Istotropic	11 A	confined	3	
			Istotropic	11 B	confined	3	
			Istotropic	11 C	unconfined	3	
6	**Schist Gneiss**	1 Direction	Oblique	12	4		

1.4.1 Augen Gneiss (AG)

The Augen Gneiss used for the tests comes from the quarry Gigler.

It is an orthogneiss, which means that it originated from magmatic rocks such as granite.

Generally speaking Augen gneiss is a coarse-grained metamorphic rock which is clotted with so called augen, large eye-shaped mineral aggregates. “Augen” is the German word for “eyes”. *[17]*

Augen Gneiss is the result from the metamorphism of granite and contains the following minerals:

Quartz (SiO_2):	40%
Feldspar ($(Ba,Ca,Na,K,NH_4)(Al,B,Si)_4O_8$):	51%
Biotite ($K(Mg,Fe)_3(AlSi_3O_{10})(F,OH)_2$):	7%
Chlorite ($(Fe,Mg,Al,Zn)_6(Si,Al)_4O_{10}(OH)_8$)	1%
Zoisite/Epidote ($Ca_2Al_3[O/OH/SiO_4/Si_2O_7]$)	1% *[18]*

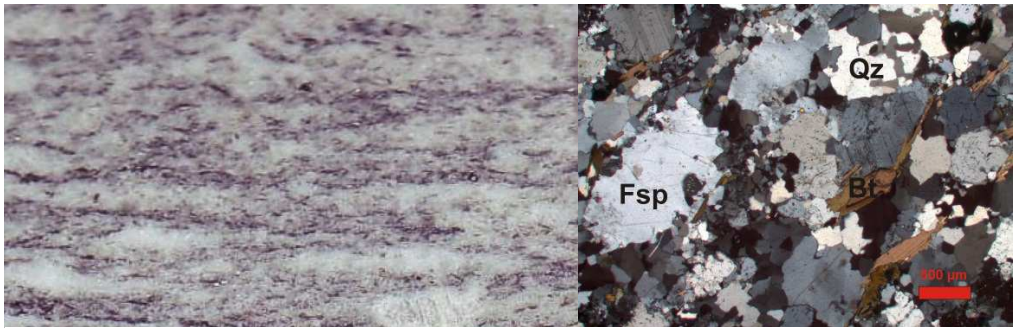

Figure 5: Macroscopic view and thin section of an Augen Gneiss ***[18]***

1.4.2 Calcareous Mica Schist (CMS)

The Calcareous Mica Schist comes from the site of a hydropower plant.

It is a crystalline metamorphic rock consisting of granular chalk, quartz and mica. The color is usually from bluish to light grey.

Calcareous Mica Schist consists of the following minerals:

Calcite ($CaCO_3$):	73%
Quartz (SiO_2):	14%
Muscovite ($KAl_2[(OH,F)_2|AlSi_3O_{10}]$):	10%
Biotite ($K(Mg,Fe)_3(AlSi_3O_{10})(F,OH)_2$):	1%
Chlorite ($((Fe,Mg,Al,Zn)_6(Si,Al)_4O_{10}(OH)_8$)	1% [18]

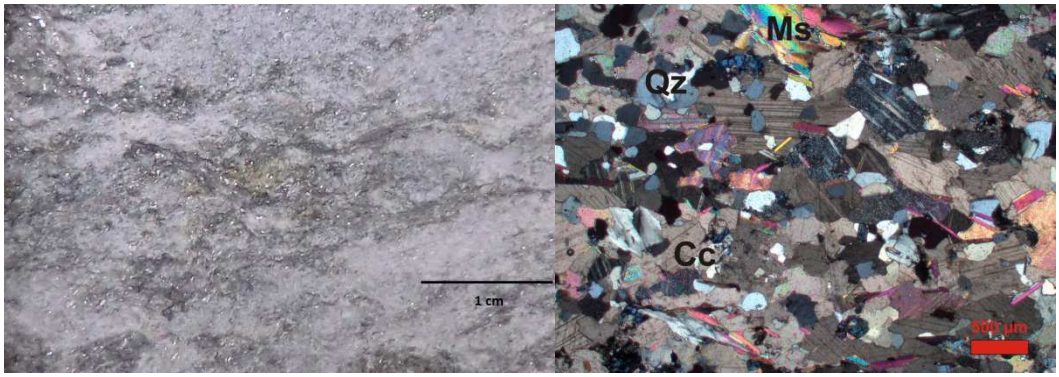

Figure 6: Macroscopic view and thin section of a Calcareous Mica Schist *[18]*

1.4.3 Granite Gneiss (GG)

Granite Gneisses are metamorphosed igneous rocks such as granites. Granites are types of intrusive, felsic, igneous rocks that are granular and crystalline in texture. The main minerals of granites are quartz, mica and feldspar. *[19]*

The examined Granite Gneiss contains these minerals:

Quartz (SiO_2):	43%
Feldspar ($((Ba,Ca,Na,K,NH_4)(Al,B,Si)_4O_8$):	46%
Biotite ($K(Mg,Fe)_3(AlSi_3O_{10})(F,OH)_2$):	8%
Chlorite ($((Fe,Mg,Al,Zn)_6(Si,Al)_4O_{10}(OH)_8$)	1%
Titanite ($CaTi[O|SiO_4]$)	1%
Zoisite/Epidote ($Ca_2Al_3[O/OH/SiO_4/Si_2O_7]$)	1% [18]

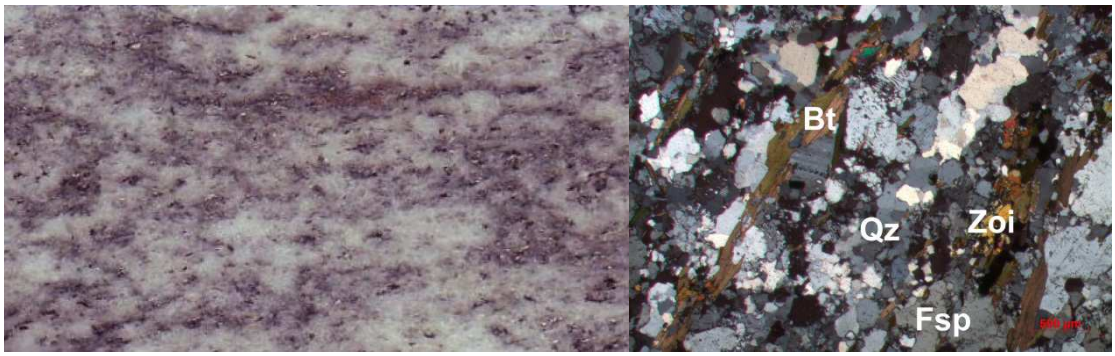

Figure 7: Macroscopic view and thin section of a Granite Gneiss *[18]*

1.4.4 Brixen Granite (BG)

The Brixen Granite used for the tests is from South Tyrol. These rocks are part of the Periadriatic fault zone, where the Brenner base tunnel tunnel will be going through.

Brixen Granite is a leucocratic rock formed during the Permian about 270 million years ago. The tectonic unit of the Brixen Granite was stressed during the Alpine orogenesis, causing brittle faults. *[20]*

The Brixen Granite consists of fine to middle grained biotite granites and granodiorites with pegmatic seams/veins. *[21]*

The evaluation of 40 thin sections revealed the following mineral content:

Quartz (SiO_2):	30-40%
Orthoclase ($KAlSi_3O_8$):	20-30%
Plagioclase ($NaAlSi_3O_8$ – $CaAl_2Si_2O_8$):	20-30%
Biotite ($K(Mg,Fe)_3(AlSi_3O_{10})(F,OH)_2$)	10-15%

[20]

Figure 8: Macroscopic view of Brixen Granite

1.4.5 Imberg Sandstone (IS)

The Imberg Sandstone is a homogenous Ruhr sandstone which was formed about 290 million years ago at the end of the Upper Carboniferous.

The distinctive features of this sandstone are its low water absorption in comparison with other sandstones, its unusual high compressive strength, its high resistance against abrasion and weathering. These are the features that made the Imberg Sandstone a demanded building and ornamental material.

Imberg Sandstone is typically light brown – a light gray or yellowish color. *[22]*

The mineral content is made up of the following minerals:

Quartz (SiO_2):	61,8%
Calcite ($CaCO_3$):	20,1%
Muscovite ($KAl_2[(OH,F)_2\|AlSi_3O_{10}]$):	5,5%
Feldspar ($(Ba,Ca,Na,K,NH_4)(Al,B,Si)_4O_8$):	12,6%

[23]

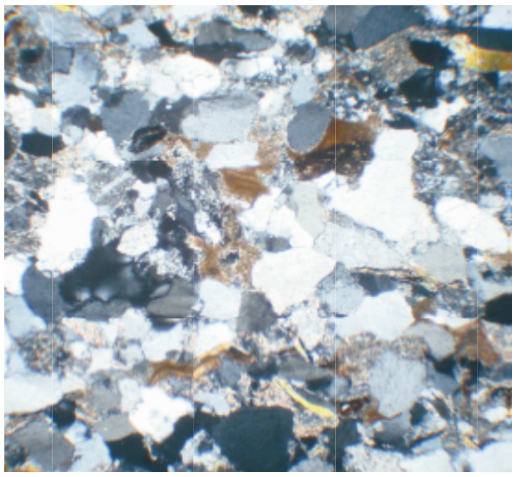

erg

1.4.6 Schist Gneiss (SG)

The Schist Gneiss used in this investigation comes from Styria.

It is a metamorphic rock formed out of sedimentary rocks under high pressures and temperatures. Schist Gneiss is a Gneiss variety in transition to phyllite.

Figure 10: Macroscopic view of Schist Gneiss

1.5 Standard geotechnical tests and LCM tests

Both standard geotechnical tests, the UCS and BTS test, were executed at laboratory of the Chair for Subsurface Engineering at the Montanuniversität Leoben. For these tests a MTS 815 servo-hydraulic press with digital feed-back control was used.

1.5.1 Uniaxial Compressive Strength - UCS

Uniaxial Compressive Strength is one of the most basic and common strength parameters of intact rock. Nearly all rock engineering applications require a determination of UCS, because it is an input parameter in almost every geotechnical calculation.

To measure the UCS of a sample, which is usually a rock core, the length to diameter ratio has to be at least 2 accoring to ÖNORM EN 1997-2 (2010 08 15) and ASTM D7012 – 10. The core is then loaded in an electronic-servo controlled stiff testing machine with a defined loading rate until it fails. The UCS is then calculated like this:

$$\sigma_c = \frac{F}{A}$$

σ_c	Uniaxial Compressive Strength (MPa)
F	Maximum failure load (kN)
A	Cross sectional area of the core sample (mm^2)

For further information regarding the sample specifications and the test execution for the UCS test there are two common guidelines:

- ÖNORM EN 1997-2 (2010 08 15): Eurocode 7 - Geotechnical design - Part 2: Ground investigation and testing
- ASTM D7012 – 10: Standard Test Method for Compressive Strength and Elastic Moduli of Intact Rock Core Specimens under Varying States of Stress and Temperatures

Some projects require more rock parameters such as the elastic modulus E and the deflection modulus V. The determination of these moduli can be performed during UCS testing, by measuring the axial ε_a and lateral deformation ε_l of the sample besides the stress.

The deflection modulus is usually determined during the first loading of the sample. The stress-strain curve is plotted and the average slope for a more or less straight line of this curve is used to calculate the deflection modulus.

$$V = \frac{\Delta\sigma}{\Delta\varepsilon_a}$$

The elastic modulus is the occurring stress difference during an unloading step referred to the variance in strain for the same segment of the curve.

For the calculation of the elastic modulus the sample is unloaded and loaded, until the difference between two consecutive axial strains is lower than 5 percent. Then the stress – strain curve for the last unloading procedure is used in the same manner as for the deflection modulus to calculate E out of it.

$$E = \frac{\Delta\sigma}{\Delta\varepsilon_a}$$

Finally the Poission's ratio can be calculated with these measured values:

$$\vartheta = -\frac{\Delta\varepsilon_a}{\Delta\varepsilon_l}$$

[24]

Figure 11 shows how an UCS test is executed. The chain around the sample is for the determination of the lateral strain, which is needed when calculating the elastic and deflection modulus.

re

The red line in Figure 12 illustrates the deflection modulus and the blue line the elastic modulus.

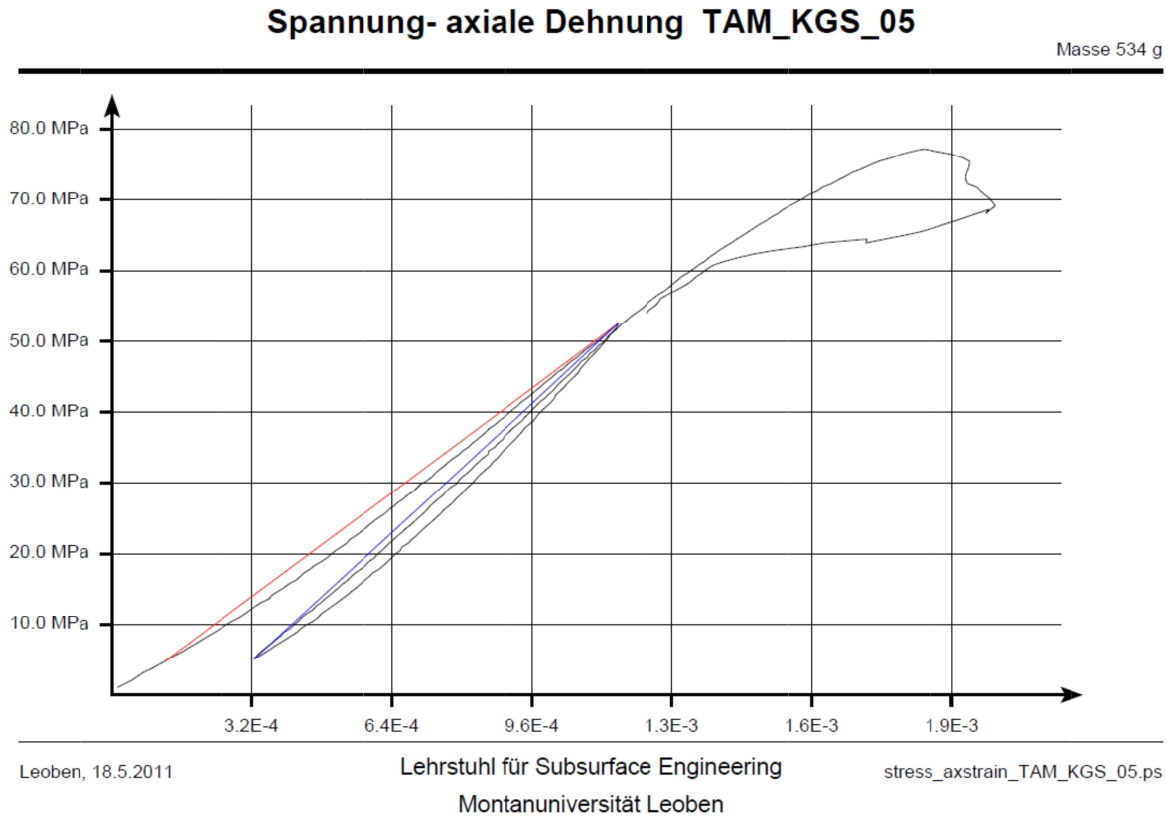

Figure 12: σ-ε diagram for an UCS test

1.5.2 Brazilian Tensile Strength - BTS

The Brazilian Tensile Strength test (BTS) is, besides the UCS test, one of the most executed geotechnical standard tests for intact rock.

The BTS determines the indirect tensile strength or split tensile strength of a rock core with a length to diameter ratio of 0,5 by measuring the load at failure. The load is applied with a defined loading rate. BTS tests are executed with the same load frames that are used for the UCS tests. The conversion from the applied load at failure into the indirect tensile strength is calculated as follows:

$$\sigma_t = \frac{2 * F}{\pi * L * D}$$

σ_t	Brazilian Tensile Strength (MPa)	
F	Maximum failure load (kN)	
L	Length of the core sample (mm)	
D	Diameter of the core sample (mm)	*[24]*

Further specifications regarding the BTS test are found in these two guidelines:

- ÖNORM B 3124-4 (1981 03 01): Prüfung von Naturstein; mechanische Gesteinseigenschaften; einaxiale Zugfestigkeit (Spaltzugfestigkeit)
- ASTM D3967 – 08: Standard Test Method for Splitting Tensile Strength of Intact Rock Core Specimens

Figure 13 shows how the BTS test is executed. One can also clearly see the failure mode during such a test.

k sample

Table 1 shows the results of all geotechnical standard tests executed at the Montanuniversität Leoben.

		UCS	BTS	E-Modulus	V-Modulus	Poisson
		[MPa]	[MPa]	[MPa]	[MPa]	[-]
Augen Gneiss	**Average**	**228,38**	**11,44**	**36716,67**	**31123,33**	**0,11**
	Variation Coefficient	0,09	0,13	0,05	0,05	0,14
	Std Dev	20,98	1,53	1786,68	1585,10	0,02
Calcareous Mica Schist	**Average**	**83,22**	**8,70**	**54516,67**	**41046,67**	**0,21**
	Variation Coefficient	0,06	0,16	0,04	0,11	0,03
	Std Dev	5,20	1,41	2200,96	4367,38	0,01
Granite Gneiss	**Average**	**132,25**	**10,26**	**41716,67**	**33463,33**	**0,15**
	Variation Coefficient	0,32	0,17	0,05	0,13	0,23
	Std Dev	42,55	1,76	1980,16	4206,36	0,04
Brixen Granite	**Average**	**140,85**	**7,84**	**38100,00**		
	Variation Coefficient	0,25	0,27	0,26		
	Std Dev	35,19	2,10	10096,48		
Imberg Sandstone	**Average**	**137,02**	**11,94**	**31722,00**	**26044,00**	**0,12**
	Variation Coefficient	0,08	0,05	0,09	0,12	0,04
	Std Dev	10,96	0,60	2835,67	3131,97	0,01
Schist Gneiss	**Average**	**81,43**	**11,01**	**59520,00**	**54,10**	**0,15**
	Variation Coefficient	0,54	0,82	0,36	0,39	0,33
	Std Dev	44,27	9,01	21320,00	21,13	0,05

Table 1: Results of geotechnical standard tests

1.5.3 Linear Cutting Machine tests - LCM

The linear cutting tests were performed both in Austria, in cooperation with Sandvik Mining and Construction G.m.b.H. in Zeltweg, and in the USA at the Earth Mechanics Institute (EMI) of the Colorado School of Mines.

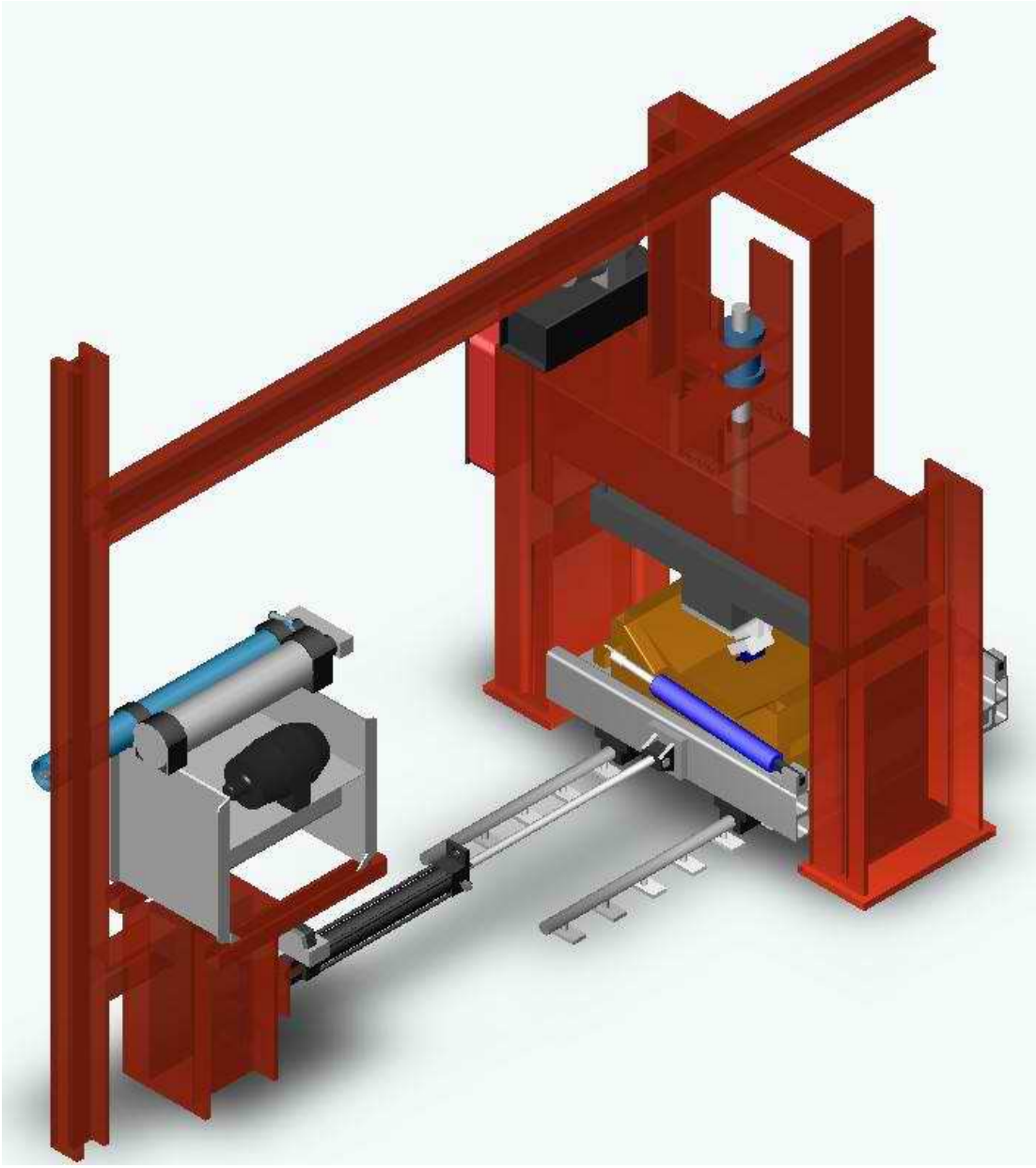

Figure 14: Linear cutter at the CSM *[25]*

Two lithologies, Granite Gneiss and Imberg Sandstone, were cut in Austria and four lithologies, Augen Gneiss, Calcareous Mica Schist, Brixen Granite and Schist Gneiss were cut in the United States.

The cutter of the LCM is mounted on a large stiff reaction frame. Between the disc cutter and the frame is a triaxial load cell monitoring normal, rolling and side forces. The movement of the rock box is recorded by a linear variable displacement transducer (LVDT). During the test the rock box is moved through the cutter at a defined constant speed, penetration and spacing to the adjacent cut. The load cell measures and records the forces acting on the cutter. *[14]*

There are differences between the two linear cutting test rigs that have to be considered in the evaluation of the results.

The first thing is the confinement of the rock blocks.

In each rock box three rock cubes with an edge length of 30 cm are placed next to each other. This means that the maximum cutting length for one pass is approximately 90 cm.

At the CSM the rock samples are cast in concrete within a steel box to provide sufficient confinement during the testing, because high forces are acting on the blocks during one run.

The rock samples at the LCM of Sandvik are mounted with heavy steel plates into a steel box, which also provides good confinement, but the rock blocks can still move for a few millimeters during the tests. The result is that this kind of confinement is less effective than the one at the CSM.

The second thing is the extent of measured forces during the test:

In comparison to the CSM LCM which has a triaxial load cell that measures normal, rolling and side forces, the LCM in Zeltweg just measures normal forces. The problems with these restricted records are that the rolling forces have to be estimated and that a comparison of the six lithologies with a performance prediction model has to be limited to normal forces.

The third things are the geometrical parameters regarding the size of the disc cutter, the spacing and the penetration depth:

The disc cutter at the CSM is a typical cutter used on actual TBMs. It has a diameter of 17 inch and a tip width of 5/8 of an inch.

The disc cutter used in Zeltweg has a diameter of 10 inch and a tip width of ½ an inch.

As penetration depth 5,08 and 7,62 mm were used in the US, but in Austria those values were 5 and 7 mm. This is because in the United States everything is measured in imperial units. Consequently, 0,2" (=5,08 mm) and 0,3" (=7,62 mm) were used.

The spacing used for all lithologies was generally 60 mm, except for Brixen Granite, where a spacing of 80 mm was used.

All those geometrical parameters are unified in the course of the use of the Colorado Schools of Mines model as the basis for an improved model, in which the PPT plays an essential role instead of the UCS and BTS tests.

A table with the average values and the according geometric parameters for all linear cutting tests executed both at the Colorado School of Mines and at the Sandvik laboratory in Zeltweg can be found in the annex.

	Direction	BETA	ALPHA	Disc Radius [mm]	Tip width [mm]	Spacing [mm]	Penetration [mm]	FN mean [kN]	FR mean [kN]	FS mean [kN]	SE mean [kNcm/cm³]
Augengneiss	Perpendicular	89	19	215,90	15,88	60	5,08	108,20	22,62	-5,29	7,45
	Perpendicular	89	19	215,90	15,88	60	7,62	154,66	21,95	5,98	4,50
	Parallel	2	18	215,90	15,88	60	5,08	78,49	14,23	0,45	4,69
	Parallel	2	18	215,90	15,88	60	7,62	135,04	17,93	8,18	3,71
	Oblique	20	40	215,90	15,88	60	5,08	68,97	14,83	-5,47	4,88
	Oblique	20	40	215,90	15,88	60	7,62	131,37	22,45	-3,58	4,93
Calcerous Mica Sc	Perpendicular	90	1	215,90	15,88	60	5,08	109,64	18,55	0,89	6,12
	Perpendicular	90	1	215,90	15,88	60	7,62	179,75	24,42	9,53	5,36
	Parallel	0	1	215,90	15,88	60	5,08	57,78	12,56	-5,00	4,13
	Parallel	0	1	215,90	15,88	60	7,62	117,37	17,66	1,49	3,87
	Oblique	20	38	215,90	15,88	60	5,08	64,61	13,98	-4,64	4,60
	Oblique	20	38	215,90	15,88	60	7,62	107,54	18,48	-2,47	4,05
Granite Gneiss	Perpendicular	90	0	127,00	12,70	60	5,00	95,05			
	Perpendicular	90	0	127,00	12,70	60	7,00	96,94			
	Parallel	0	0	127,00	12,70	60	5,00	55,43			
	Parallel	0	0	127,00	12,70	60	7,00	57,12			
	Oblique		45	127,00	12,70	60	5,00	74,69			
	Oblique		45	127,00	12,70	60	7,00	81,66			

	Block Size										
Brixen Granite	B5			215,90	15,88	80,00	1,27	25,02	6,43	-2,79	5,30
	B5			215,90	15,88	80,00	2,54	58,35	11,99	0,64	4,93
	B5			215,90	15,88	80,00	3,81	71,99	14,52	-2,14	3,98
	B5			215,90	15,88	80,00	5,08	91,29	19,19	-4,92	3,95
	B5			215,90	15,88	80,00	6,35	113,06	19,29	3,62	3,18
	B10			215,90	15,88	80,00	1,27	78,49	17,09	-0,12	14,07
	B10			215,90	15,88	80,00	2,54	80,99	16,67	-0,74	6,86
	B10			215,90	15,88	80,00	3,81	106,79	18,36	4,54	5,04
	B10			215,90	15,88	80,00	5,08	145,03	23,90	3,05	4,92
	B10			215,90	15,88	80,00	6,35	160,39	25,92	2,92	4,27
	B20			215,90	15,88	80,00	1,27	89,14	17,87	0,56	14,71
	B20			215,90	15,88	80,00	2,54	81,80	13,95	4,01	5,74
	B20			215,90	15,88	80,00	3,81	130,91	21,95	0,60	6,02
	B20			215,90	15,88	80,00	5,08	139,55	22,02	3,03	4,53
	B20			215,90	15,88	80,00	6,35	170,86	22,76	13,80	3,75
	B30			215,90	15,88	80,00	1,27	52,47	14,37	-10,84	11,83
	B30			215,90	15,88	80,00	2,54	73,42	13,59	-3,55	5,59
	B30			215,90	15,88	80,00	3,81	98,93	19,45	-10,48	5,34
	B30			215,90	15,88	80,00	5,08	130,64	21,59	-1,41	4,44
	B30			215,90	15,88	80,00	6,35	158,62	26,45	-0,93	4,35
	B40			215,90	15,88	80,00	1,27	58,81	14,35	-2,70	11,81
	B40			215,90	15,88	80,00	2,54	74,45	14,61	-3,27	6,01
	B40			215,90	15,88	80,00	3,81	91,22	14,94	3,32	4,10
	B40			215,90	15,88	80,00	5,08	101,32	18,70	-0,81	3,85
	B40			215,90	15,88	80,00	6,35	121,38	21,22	-0,23	3,49
	Average			215,90	15,88	80,00	1,27	60,79	14,02		
	Average			215,90	15,88	80,00	2,54	73,80	14,16		
	Average			215,90	15,88	80,00	3,81	99,97	17,85		
	Average			215,90	15,88	80,00	5,08	121,56	21,08		
	Average			215,90	15,88	80,00	6,35	144,86	23,13		

	Block Size										
Imberg Sandstone	B30			127,00	12,70	60	3,00	67,09			
	B30			127,00	12,70	60	5,00	52,98			
	B30			127,00	12,70	60	7,00	53,06			
	B60			127,00	12,70	60	3,00	95,01			
	B60			127,00	12,70	60	5,00	66,93			
	B60			127,00	12,70	60	7,00	70,58			
	Big Block			127,00	12,70	60	3,00	104,10			
	Big Block			127,00	12,70	60	5,00	113,56			
	Big Block			127,00	12,70	60	7,00	111,37			
	Average			127,00	12,70	60	3,00	88,73			
	Average			127,00	12,70	60	5,00	77,82			
	Average			127,00	12,70	60	7,00	78,34			

SG	Oblique	10	50	215,90	15,88	60	5,08	101,19	19,35	1,39	6,37
	Oblique	10	50	215,90	15,88	60	7,62	126,54	20,44	2,73	4,47

Table 2: Results of the conducted linear cutting tests

2. Main part

2.1 PPT: Testing Methodology

2.1.1 Sample preparation – drilling, sawing (Montanuniversitaet Leoben)

The first part of the sample preparation was done in the rock engineering laboratory of the Chair for Subsurface Engineering at the Montanuniversity Leoben. A total of 53 rock cores were prepared and sent to the CSM for PPT testing.

The desired dimensions of the rock samples were cylindric rock cores with a diameter of 54 mm and a length of 70 mm and a saw-cut surface.

This part aimed at getting rock cores out of the original rock blocks. There was at least one rock block with an edge length of 30 cm for each lithology. For those lithologies where an oblique direction of foliation was needed, a second block was required. This is because of the clamp while drilling, which could only be ensured with the drilling bit perpendicular to the rock surface.

After drilling the rock cores, which usually had a length of 30 cm, they were cut into pieces with a length slightly over 70 mm. This additional length was needed in case the two surfaces of the cylinder were not parallel to each other and the sample had to be ground.

Figure 15: Preparation of rock cores

2.1.2 Sample preparation – casting, grinding (Colorado School of Mines)

For testing the rock cores with the punch penetration test, they need to be confined. This is achieved by putting the core into a steel ring of 82 mm inner diameter and filling the remaining space with Hydrostone to ensure good confinement.

This procedure simulates the partially confined conditions at the tunnel face and ensures that the rock sample does not fail prematurely by tensile splitting, but crushing and chip formation occurs as it does while disc cutting.

Hydrostone is a gypsum cement with a high compressive strength of up to 69 MPa and a small setting expansion of 0,24%, which provides an additional confining pressure on the sample. The recommended consistency for mixing the Hydrostone is achieved by using 32 parts of water by weight per 100 parts of plaster.

For the testing program 9 steel rings with an inner diameter of 82 mm, an outer diameter of 102 mm and a wall thickness of 10 mm were prepared. With those nine rings two lithologies, consisting of four or five samples each, could be casted at once.

Before starting the casting procedure the steel rings are cleaned on the inside with a wire brush to remove the old parts of Hydrostone from the last tests. Next the rings are put on a smooth and even surface with the rock cores in the center of them. Then the prescribed amounts of water and Hydrostone are weighed and mixed. After that the slurry is poured carefully into the remaining circular gap between the rock core and the steel ring to prevent air bubbles and provide a uniform mixture. Finally the plaster is left to set for at least two days.

After these two days the overcoming Hydrostone is removed by grinding with a milling machine. The grinding ensures a smooth and flat surface for the bottom side of the sample so that the surface of the rock core on the top side is exactly parallel to the horizontal steel plates of the PPT testing machine perpendicular to the indenter.

Figure 16: Casting and grinding of the PPT samples

2.1.3 Testing Procedure

The testing equipment for the punch penetration test consists of a hydraulic power unit, a very stiff load frame with a loading capacity of approximately 270 tons, a control box and a computerized control and data acquisition system. All parts are manufactured, serviced and calibrated by MTS Systems Corporation.

The testing procedure starts by putting the prepared samples into the load frame. After that the hydraulic ram is carefully moved upwards until the rock surface touches the conical shaped tungsten carbide indenter, which is mounted on the top side of the load frame. The conical indenter has a tip angle of 120° and a tip radius of 3,175 mm. Then a preset and defined loading procedure is started, which moves the steel plates on which the PPT sample is standing, up with a constant speed of 0,0254 mm/s. While performing the test, the applied force and the displacement of the indenter into the rock surface are monitored and recorded every 0,25 seconds. The test is stopped automatically when the abort criterion, a penetration of 6,35 mm into the rock, is reached.

Finally the result is a force-penetration graph. All measured values, i.e. time, penetration and applied force, which are measured four times per second can be exported into an EXCEL-sheet for further processing.

To evaluate the failure mode and the damages to the rock, it is important to take “before” and “after” pictures of the samples.

Punch Penetration Test Indentor

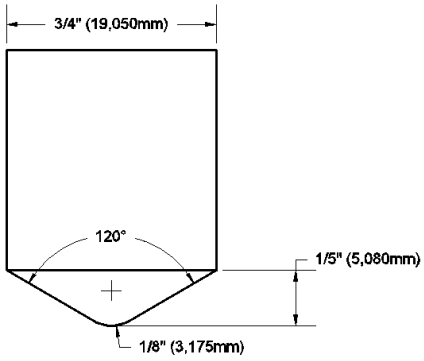

Figure 17: MTS testing equipment and a close-up view of the indentor

2.1.4 MTS Station Manager / Data Acquisition

MTS provides all the software and hardware for controlling the load frame and the hydraulic equipment. The Station Manager (Figure 19) on the computer used for monitoring the tests enables the qualified user to steer the hydraulic ram, create procedures with self-defined loading rates, abort criteria, signals to be measured, recorded and plotted, change the unit assignment and a lot more (Figure 18).

After starting the Station Manager the procedure for the kind of test that is going to be performed next is selected. There are preset procedures for all kinds of rock tests, for example UCS, BTS, PPT and Triaxial Compressive Strength.

Another thing that should not be forgotten before starting a test run is to set all the measured channels to zero to have no offset. Of course it is possible to correct that after the test as well, but it is a lot more work afterwards.

Exporting the measured data into an Excel-sheet is really easy. The test data is saved as ".dat" file and formatted in a way, that if it is opened in Excel each measured channel is written in a single row. Now you just need to copy the current sheet into a new Excel file or save it as a new Excel file, which is in fact even easier.

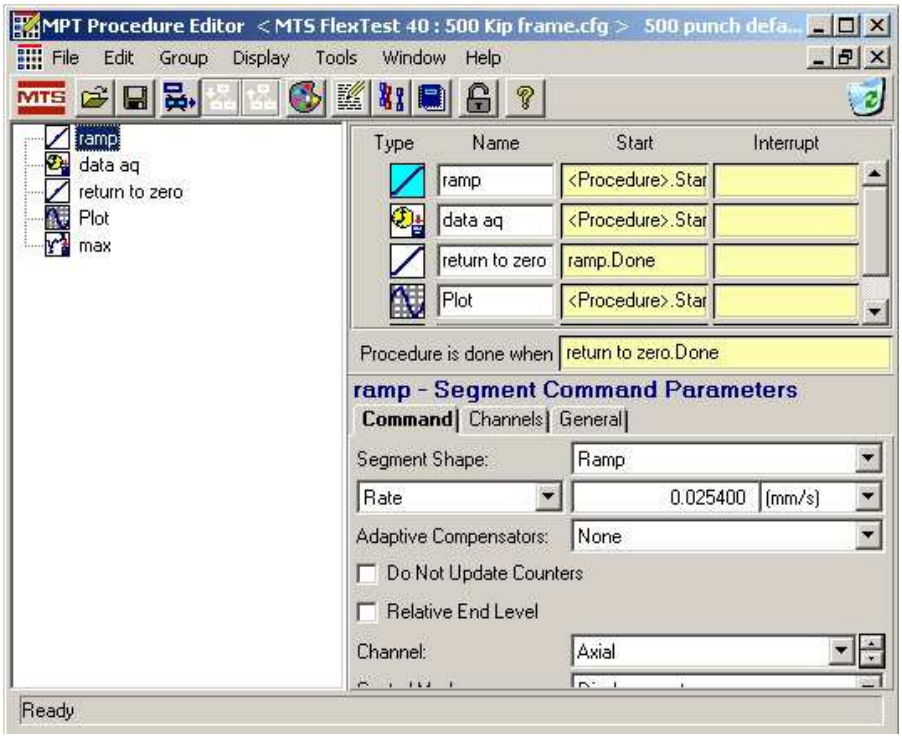

Figure 18: Procedure Editor

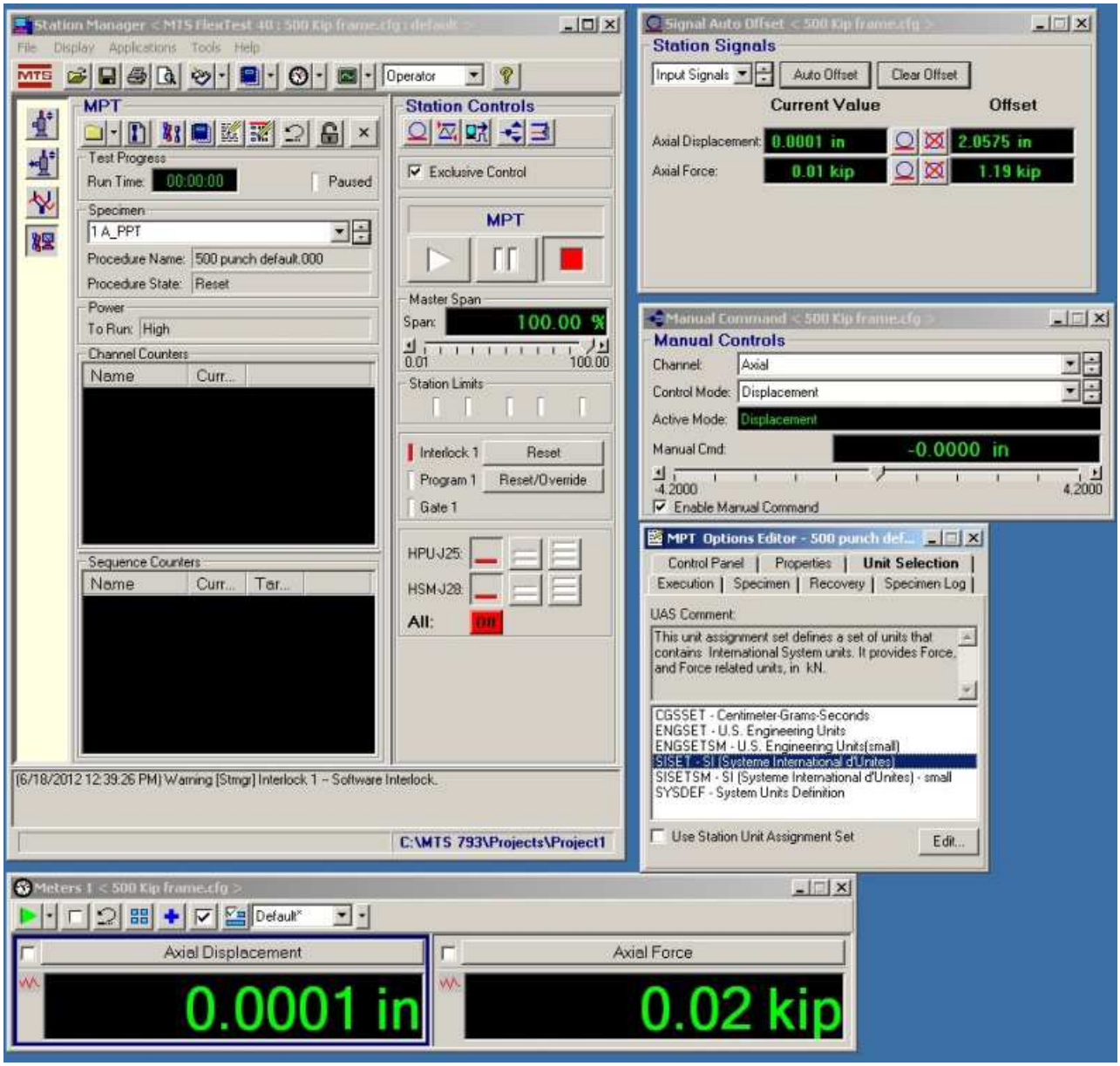

Figure 19: MTS Station Manager

2.1.5 Summary sheets

Table 3 shows a summary sheet for the post-processing of a punch penetration test. Especially the “before” and “after” pictures are essential for storing the files, because of the failure assessment if the samples are not available anymore.

Punch Penetration Test					
Project:	Diploma Thesis ERBEN				
Rock Type:	Augengneiss (Perpendicular)				
Core ID:	1 A		**Data file:**	1 A	
Characteristics:					
Sample Length:	**71,7**	mm	**Diameter:**	**54,66**	mm
Sample Weight:	**441,02**	g	**Density:**	**8,23**	g/cm³
Loading Rate:	**0,0254**	mm/s			
Maximum Load:	**194,94**	kN	**@ Penetr.:**	**5,67**	mm
Operator:	**HE**		**Date:**	**10.04.2012**	
Comments:	Video; meaningful until 5.1 mm;				

Table 3: Summary sheet of a Punch Penetration Test

2.2 Results of the PPT

2.2.1 Data processing: from raw data to graphs and characteristic points

The exported raw data consists of three columns which represent the three measured channels for the standard PPT, time (sec), axial displacement (mm) and axial force (kN) (Figure 21). Each punch penetration test lasts about 250 seconds, with four values per second, which is a total of approximately 1000 measured values per column.

At the bottom of the data sheet is a short summary, giving the maximum load that occurred during the test, the associated displacement of the indenter at that time and the overall duration of the experiment. This is useful for checking the results after reducing the data, although there is always a tiny difference between the two data sets, because of a small offset that has to be eliminated during the reduction. This offset comes from a natural fluctuation in the measuring channels, which can never be completely extinguished.

For reducing the collected raw data a new Excel template was developed.

The first thing the file does, is reducing the inserted raw data by eliminating the offset. With this reduced data a diagram is created, showing the force-penetration graph.

The next objective is to find characteristic points. For this study three characteristic points were investigated in terms of consistency and variation within each lithology and loading direction: the point of first failure (FF), the point of the maximum force until 3,5 mm (3,5) and the point where the maximum load during the entire test occurs.

	A	B	C	D
1	MTS793|MPT|ENU|1|2|.|/|:|1|0|0|A			
2				
3	Data Acquisition			punch per
4	Time	Axial Disp	Axial Force	
5	Sec	mm	kN	
6	0,306641	-0,00146	1,708846	
7	0,556641	-2,57E-05	1,868285	
8	0,806641	0,001792	1,987595	
9	1,056641	0,005009	2,116749	
10	1,306641	0,008664	2,223572	
11	1,556641	0,012957	2,291122	
12	1,806641	0,017831	2,400489	
13	2,056641	0,023778	2,4783	
14	2,306641	0,029484	2,598804	
15	2,556641	0,035379	2,658777	
16	2,806641	0,041568	2,73788	
17	3,056641	0,047205	2,765063	
18	3,306641	0,053545	2,803819	
19	3,556641	0,0597	2,744541	
20	3,806641	0,066217	2,780534	

Figure 21: PPT raw data

The term first failure, or first fracture, is used to describe the point at which a loud noise was observed along with the first sign of a significant failure event, such as a crater formation and chip generation.

Penetration at First Failure: is the measured penetration depth of the indenter into the rock when the first failure occurs.

Load at First Failure: is the measured load acting on the indenter when the first failure occurs. *[7]*

The criterion for the first failure point is that it is a local extreme and the force at this point has to be higher than the measured value for the previous and the six following points and that the force of the point immediately after the FF is at least lower than 99,5% of the value at FF. In Excel this condition looks like this:

*"=IF(AND(G51<G50*0,995;G50>G49;G50>G51;G50>G52;G50>G53;G50>G54;G50>G55;G50>G56); G50; 0)"*

If a point fulfills all conditions it is the point of first failure and the corresponding force and penetration are written into the summary table below the diagram.

The maximum forces and the associated penetration depths until 3,5 mm penetration and for the entire test are easy to find by using the MAX-function. The results are again written into the summary table.

Another value that was paid attention was the energy consumption for penetrating until 3,5 mm and until 6,35 mm. The codes for implementing those conditions and calculating the total energy out of it look like this:

"=IF(AND(F50-F49>0;F50-F49<0,1);F50-F49;0)" *[mm]*

*"=G50*1000*J50/1000"* *[J]*

"=SUM(K50:K1062)" *[J]*

The first line is for determining the length of each measured step. The second line is for multiplying the length of a step with the actual measured force during this step resulting in the energy for one single step. The third line is for summing up all the single steps to get the total energy consumption.

Two other parameters were calculated for finding a characteristic value that represents the result of the PPT.

The first one was the specific energy (SE) by dividing the total energy (E_t) by the volume of debris (V_{deb}). The volume of the crushed rock was determined by weighing the mass of the debris (m_{deb}) after the test and calculating its volume by dividing the mass by its density (ρ), which was determined for each single rock core.

$$SE = \frac{E_t}{V_{deb}}$$

$$V_{deb} = \frac{m_{deb}}{\rho}$$

The second one was the specific penetration (SP), which was calculated by dividing the measured forces (F) at a certain point by the corresponding penetration (p).

$$SP = \frac{F}{p}$$

The following Excel-sheet shows the summary of the results for all tests of one lithology and was created for a better overview (Table 4). The sheet below depicts the data reduction sheet for a single test with all the calculated values discussed above (Table 5).

1 **Augen Gneiss - Perpendicular**

	First Failure			3,5				Maximum			Total	
	Load	@ Penetration	SP	Load	@ Penetration	SP	Energy	Load	@ Penetration	SP	Energy	SE
	[kN]	[mm]	[kN/mm]	[kN]	[mm]	[kN/mm]	[J]	[kN]	[mm]	[kN/mm]	[J]	[J]
1 A	15,56	0,7086	21,96	67,59	2,057	32,86	99,85	193,13	5,6741	34,04	453,49	223,39
1 B	19,39	0,6537	29,67	120,68	3,214	37,55	159,17	183,29	5,4400	33,69	505,89	337,26
1 C	24,66	0,7885	31,28	158,30	3,489	45,37	171,34	220,55	5,5967	39,41	655,70	437,14
1 D	20,81	0,7219	28,83	143,07	3,496	40,93	181,32	182,29	5,0705	35,95	488,37	325,58
Average	20,11	0,72	27,94	122,41	3,06	39,18	152,92	194,82	5,45	35,77	525,86	330,84
Variance	14,13	0,00	16,88	1574,31	0,47	27,97	1334,02	318,32	0,07	6,86	7967,08	7637,48
Standard deviation	3,76	0,06	4,11	39,68	0,68	5,29	36,52	17,84	0,27	2,62	89,26	87,39
CV (coeff. of variati	**0,19**	**0,08**	**0,15**	**0,32**	**0,22**	**0,13**	**0,24**	**0,09**	**0,05**	**0,07**	**0,17**	**0,26**

Table 4: Result overview for Augen Gneiss penetrated normal to the foliation

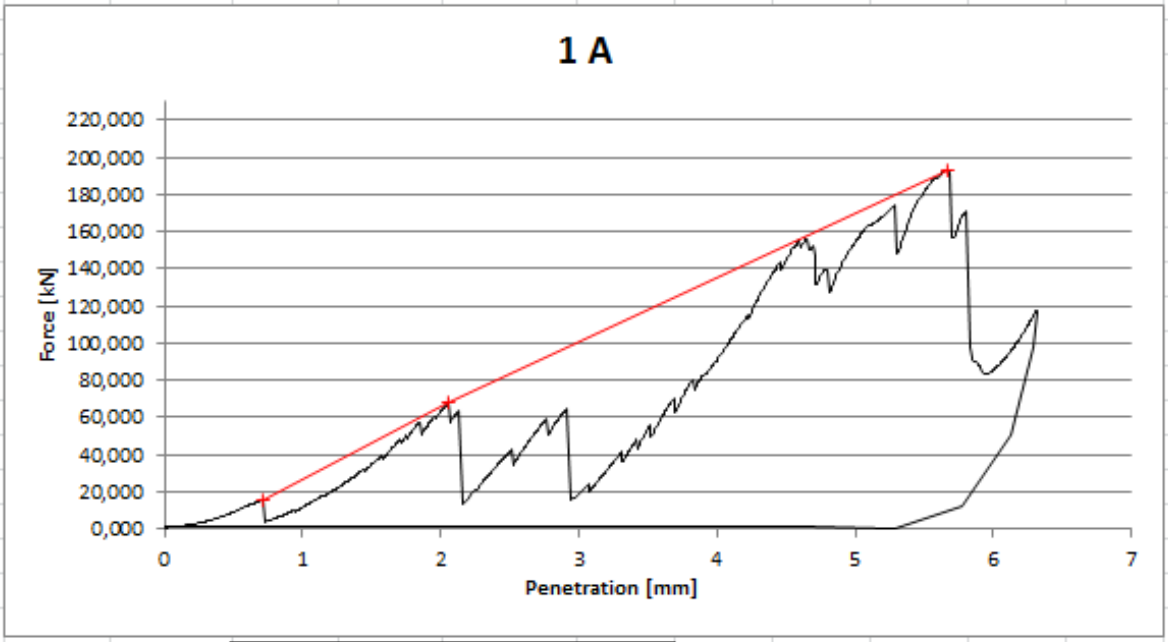

	Force kN		@ Penetration mm	
First Failure Load	15,564		0,709	
Max Laod 3.5 mm	67,590		2,057	
Maximum Load	193,128		5,674	
Energy (3.5mm/total)	99,847	[J]	453,489	[J]
Specific Energy			223,393	[MJ/m³]
Volume of Debris	2,03	[cm³]		

3,5

1 A										
Original Data			Reduced Data		Force		Energy			
Time	Axial Displa	Axial Forc	Axial Disp	Axial Force	FF	3,5	total		3,5	
[Sec]	[mm]	[kN]	[mm]	[kN]	[kN]	[kN]	[mm]	[J]	[mm]	[J]
0,307	-0,001	1,709	0,000	0,000	0	0,000				
0,557	0,000	1,868	0,001	0,159	0	0,159	0,001	0,000	0,001	0,000
0,807	0,002	1,988	0,003	0,279	0	0,279	0,002	0,001	0,002	0,001
1,057	0,005	2,117	0,006	0,408	0	0,408	0,003	0,001	0,003	0,001
1,307	0,009	2,224	0,010	0,515	0	0,515	0,004	0,002	0,004	0,002
1,557	0,013	2,291	0,014	0,582	0	0,582	0,004	0,003	0,004	0,003
1,807	0,018	2,400	0,019	0,692	0	0,692	0,005	0,003	0,005	0,003
2,057	0,024	2,478	0,025	0,769	0	0,769	0,006	0,005	0,006	0,005
2,307	0,029	2,599	0,031	0,890	0	0,890	0,006	0,005	0,006	0,005
2,557	0,035	2,659	0,037	0,950	0	0,950	0,006	0,006	0,006	0,006
2,807	0,042	2,738	0,043	1,029	0	1,029	0,006	0,006	0,006	0,006
3,057	0,047	2,765	0,049	1,056	0	1,056	0,006	0,006	0,006	0,006
3,307	0,054	2,804	0,055	1,095	0	1,095	0,006	0,007	0,006	0,007

Table 5: Data reduction sheet for a single test

2.2.2 Evaluation of results: comparison of characteristic points and graphs

One of the aims of this thesis is to find a point or value that is characteristic for the punch penetration test. This could either be the point of first failure (establishment of first chips and drop in force), or a point after a few Millimeters (when the indenter is in full interaction with the rock), or the point of maximum force. There has been a lot of effort in the last years to find such a point.

Yagiz for example suggested to use the following equation for determining an index value for brittleness out of the PPT:

$$BI_m = \frac{F_{max}}{P}$$

BI_m	Brittleness Index (kN/mm)
F_{max}	Maximum applied force (kN)
P	Corresponding penetration (mm) *[5]*

This Brittleness Index is nothing really new, because it is in fact the same characteristic value that has been used by the Earth Mechanics Institute of the Colorado School of Mines to reduce their PPT data since 1999.

An Excel macro was utilized to reduce the data and calculate the so called Peak Slope Index, which was determined by dividing the maximum load by the corresponding penetration of the indenter. *[13]*

$$PSI = \frac{L_{max}}{P_C}$$

PSI	Peak Slope Index
L_{max}	Maximum load (kN)
P_C	Corresponding penetration (mm) *[26]*

This point is a pretty good parameter, but there are a few problems while obtaining the data for the calculation of this index:

The first and most important problem is that at a penetration depth of 3,5 mm the accumulating rock chips start to pile up between the rock surface and the steel plate on which the indenter is mounted. This leads to an interference of the penetration process:

The measured force in the system is increased, because the crushing process between the sample and the rock surface is measured as well and therefore the stress at the indenter for penetrating the rock is overestimated and not as high as the calculation would suggest.

Of course this restraint is not too critical, but it is a systematic measuring error occurring after a penetration of 3,5mm, which can definitely be measured and influences the results.

The second thing is that there is a different gradient in the lines for the first failure point and the PSI. Investigations for this thesis have shown that specific penetration which is an indicator for the gradient and the same as the PSI and the BI_m, for the FF point is always below the SP for the maximum force.

The explanation for this observation is hard to explain. The first chipping process takes less energy than the following, although the rock is intact at this stage. On the other hand the following formation of rock chips needs more energy, although the rock core gets more and more fractured and weaker. These two observations can be explained by the increasing depth of penetration and the size of chips formed. With the progressing penetration, the indenter surface covered by rock gets larger and larger. Therefore it takes more and more energy to keep up the same penetration rate. With the increasing depth of penetration also the size of chips formed, gets bigger. The result of a growing chip size and an increasing indenter footprint is also a rising force and energy consumption of the system.

However when performing a PPT we are interested in the forces and amount of energy that it takes to form chips at the beginning of the penetration, because after a certain penetration depth side effects start to dominate the failure process. Among those side effects is the interfered movement of the indenter after about 3,5mm and what is more important the decreasing confining effect of the Hydrostone which can be explained by cracks running through the rock sample and the Hydrostone.

During the tests it was recognized that this certain penetration depth, when the rock core fails in the middle and the cracks are running through the Hydrostone as well, is between 3 and 4 mm. This observation can also be consolidated by having a deeper look on the force-penetration graphs of all tests. Usually there is a peak in the graph in this certain area and after this peak force decreases dramatically and after that it nearly takes about a millimeter to reach the previous value before this outstanding failure. It takes such a long way for the force to increase again, because through the cracking there is much less resistance of the rock against further penetration.

The rise in force after this point can easily be explained because the rock and the Hydrostone remain in place, but it simply takes one millimeter for the material to be compacted again and be able to take stress.

This peak and the following drop in force can be explained by a major failure event causing deep cracks in the sample and splitting the rock core in the middle. The graphs below clearly show this force drop marking the destruction of the rock core.

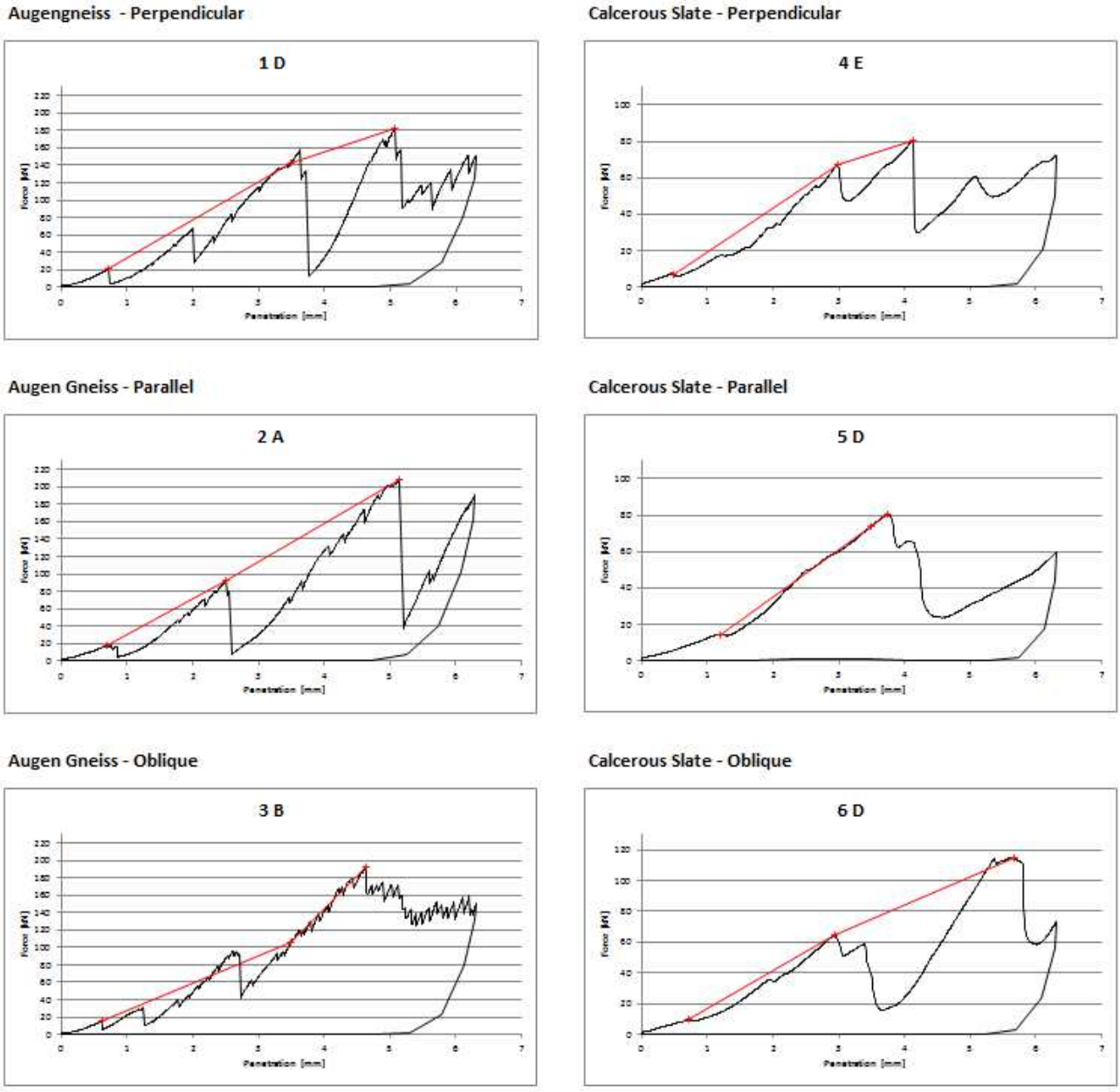

Figure 22: Characteristic force-penetration graphs (1)

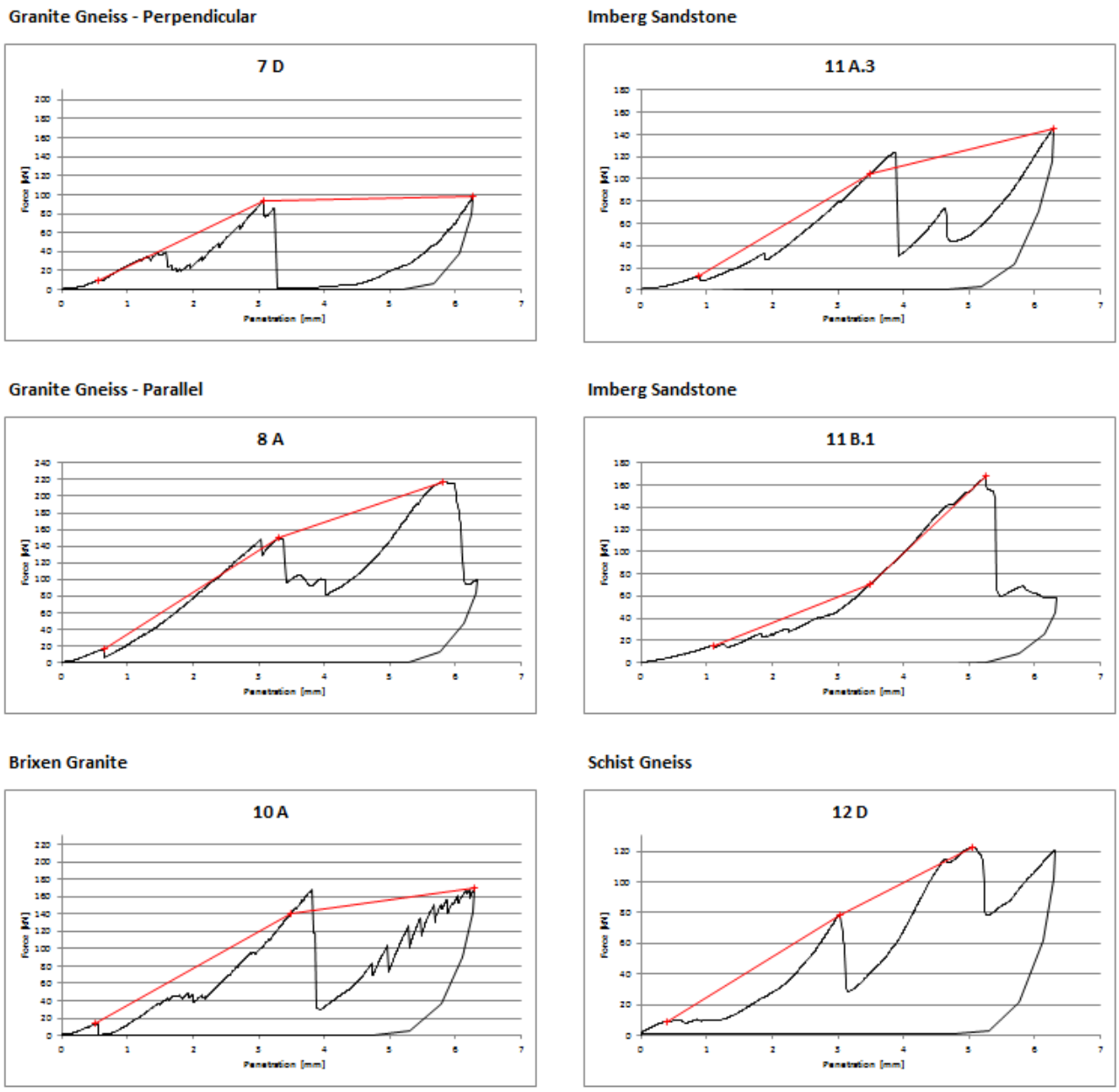

Figure 23: Characteristic force-penetration graphs (2)

To use data after this point is not really reliable and therefore the First Failure Point is used as the basis for the establishment of an index describing the PPT with a single value.

There were also attempts to find a characteristic point at around 3,5 mm, but the standard deviation and the coefficient of variation were simply too high for such a point and the procedure could not be automated.

The following tables (Table 6, Table 7, Table 8, Table 9 andTable 10) show a summary for all conducted PPT. For each single test the following key parameters were listed or calculated. How those parameters are determined was already explained in the previous section.

First Failure Point:

- Load
- Corresponding Penetration
- Specific Penetration (SP)

The point where the maximum force until 3,5 mm occurs:

- Load
- Corresponding Penetration
- Specific Penetration (SP)
- Energy

The point where the maximum load throughout the whole test is measured:

- Load
- Corresponding Penetration
- Specific Penetration (SP)

Further the whole energy consumption and the specific energy during the test was calculated.

- Energy
- Specific Energy (SE)

Within each lithology at least four tests were carried out for each loading direction in addiction to the foliation and assembled in a group from 1 to 12. For those four tests average, variance, standard deviation and coefficient of variation (CV) were calculated.

Average: $\bar{x} = \frac{\sum_{i=1}^{n} x_i}{n}$

Variance: $\hat{\sigma}^2 = \frac{\sum_{i=1}^{n} (x_i - \bar{x})^2}{n-1}$

This formula for calculating the variance is used when calculating the variance of a sample of a population (analytic statistic), when the entire population is unknown. When

determining rock properties it is not realistic to measure a parameter for ALL existing types of rock and this is why the formula for the sample variance is used.

Standard deviation: $\hat{\sigma} = \sqrt{\hat{\sigma}^2}$

Coefficient of variation: $CV = \frac{\hat{\sigma}}{\bar{x}}$

The coefficient of variation (CV) is very useful for comparing more standard deviations with each other. In this thesis the CV is the main parameter for comparing the different key parameters with each other to find out, which parameter is the most consistent throughout a number of tests.

Consistency and being clear of systematic errors is the essential thing about a new index or parameter that is used as a single value for describing the result of the PPT.

At the very bottom line of the following tables is the comparison of the overall coefficients of variation for all conducted tests and compared key parameters.

			First Failure			3,5 mm				Maximum			Total					
			Load	@ Pen.	SP	Load	@ Pen.	SP	Energy	Load	@ Pen.	SP	Energy	SE	Angle	Mass of De	Volume of Deb	Density
			[kN]	[mm]	[kN/mm]	[kN]	[mm]	[kN/mm]	[J]	[kN]	[mm]	[kN/mm]	[J]	[J/g!!!]	[°]	[g]	[cm³]	[g/cm³]
Augengneiss	Normal	1 A	15,56	0,7086	21,96	67,59	2,057	32,86	99,85	193,13	5,6741	34,04	453,49	71,06	40,00	16,720	6,38	2,62
		1 B	19,39	0,6537	29,67	120,68	3,214	37,55	159,17	183,29	5,4400	33,69	505,89	72,47	36,00	18,290	6,98	2,62
		1 C	24,66	0,7885	31,28	158,30	3,489	45,37	171,34	220,55	5,5967	39,41	655,70	63,42	45,00	27,090	10,34	2,62
		1 D	20,81	0,7219	28,83	143,07	3,496	40,93	181,32	182,29	5,0705	35,95	488,37	60,36	42,00	21,200	8,09	2,62
		Average	**20,11**	**0,72**	**27,94**	**122,41**	**3,06**	**39,18**	**152,92**	**194,82**	**5,45**	**35,77**	**525,86**	**66,82**	**40,75**	**20,83**	**7,95**	**2,62**
		Variance	14,13	0,00	16,88	1574,31	0,47	27,97	1334,02	318,32	0,07	6,86	7967,08	34,42	14,25	20,89	3,04	0,00
		Standard deviation	3,76	0,06	4,11	39,68	0,68	5,29	36,52	17,84	0,27	2,62	89,26	5,87	3,77	4,57	1,74	0,00
		CV (coeff. of variation)	**0,19**	**0,08**	**0,15**	**0,32**	**0,22**	**0,13**	**0,24**	**0,09**	**0,05**	**0,07**	**0,17**	**0,09**	**0,09**	**0,22**	**0,22**	**0,00**
	Parallel	2 A	17,46	0,6840	25,53	92,73	2,509	36,96	115,01	207,98	5,1378	40,48	484,64	126,49	63,00	10,000	3,83	2,61
		2 B	16,48	0,6396	25,76	115,39	3,495	33,01	151,83	171,96	5,6571	30,40	480,89	77,51	62,00	16,070	6,20	2,59
		2 C	13,75	0,5138	26,76	93,96	3,417	27,50	132,72	173,78	5,4735	31,75	489,44	77,51	50,00	16,480	6,31	2,61
		2 D	11,49	0,4924	23,34	66,58	2,922	22,78		185,64	5,8580	31,69			46,00	14,160	5,40	2,62
		Average	**15,90**	**0,61**	**26,02**	**100,70**	**3,14**	**32,49**	**133,19**	**184,57**	**5,42**	**34,21**	**484,99**	**93,84**	**58,33**	**14,18**	**5,45**	**2,60**
		Variance	3,70	0,01	0,43	162,34	0,30	22,59	339,12	411,79	0,07	29,96	18,36	799,69	52,33	13,17	1,97	0,00
		Standard deviation	1,92	0,09	0,65	12,74	0,55	4,75	18,42	20,29	0,26	5,47	4,29	28,28	7,23	3,63	1,40	0,01
		CV (coeff. of variation)	**0,12**	**0,14**	**0,03**	**0,13**	**0,17**	**0,15**	**0,14**	**0,11**	**0,05**	**0,16**	**0,01**	**0,30**	**0,12**	**0,26**	**0,26**	**0,00**
	Oblique	3 A	13,74	0,5671	24,22	119,35	3,498	34,12	129,84	201,92	5,9878	33,72	582,03	71,76	35,00	21,250	8,11	2,62
		3 B	15,09	0,6243	24,17	105,73	3,495	30,25	147,41	193,23	4,6341	41,70	565,34	60,41	45,00	24,520	9,36	2,62
		3 C	16,74	0,6570	25,48	138,32	3,495	39,58	193,17	197,25	6,3013	31,30	532,63	114,48	46,00	12,050	4,65	2,59
		3 D	13,05	0,5573	23,42	119,12	3,497	34,06	165,32	193,02	6,3060	30,61	552,86	105,96	48,00	13,670	5,22	2,62
		Average	**14,66**	**0,60**	**24,32**	**120,63**	**3,50**	**34,50**	**158,94**	**196,36**	**5,81**	**34,33**	**558,22**	**88,15**	**43,50**	**17,87**	**6,83**	**2,61**
		Variance	2,66	0,00	0,73	179,61	0,00	14,74	730,67	17,54	0,63	25,89	433,66	682,99	33,67	35,72	5,13	0,00
		Standard deviation	1,63	0,05	0,86	13,40	0,00	3,84	27,03	4,19	0,80	5,09	20,82	26,13	5,80	5,98	2,26	0,02
		CV (coeff. of variation)	**0,11**	**0,08**	**0,04**	**0,11**	**0,00**	**0,11**	**0,17**	**0,02**	**0,14**	**0,15**	**0,04**	**0,30**	**0,13**	**0,33**	**0,33**	**0,01**

Table 6: Result overview PPT (1)

			First Failure			3.5 mm				Maximum			Total					
			Load	@ Pen.	SP	Load	@ Pen.	SP	Energy	Load	@ Pen.	SP	Energy	SE	Angle	Mass of De	Volume of Deb	Density
			[kN]	[mm]	[kN/mm]	[kN]	[mm]	[kN/mm]	[J]	[kN]	[mm]	[kN/mm]	[J]	[J/g!!!]	[°]	[g]	[cm³]	[g/cm³]
Calcerous Slate (Kalkglimmerschiefer)	Normal	4 A	2,23	0,1635	13,61	34,61	2,485	13,93	47,39	56,46	6,2791	8,99	151,53	22,31	14,00	18,47	6,79	2,72
		4 B	4,23	0,2658	15,93	61,93	3,499	17,70	72,94	62,55	3,5239	17,75	164,28	18,70	14,00	23,90	8,79	2,72
		4 C	4,35	0,2655	16,37	62,50	3,497	17,87	79,20	101,11	5,2152	19,39	303,11	30,52	15,00	26,62	9,93	2,68
		4 D	5,39	0,3918	13,75	50,23	3,499	14,35	64,46	62,61	5,8479	10,71	197,95	24,69	13,00	21,89	8,02	2,73
		4 E	6,71	0,4928	13,62	67,41	2,985	22,58	103,68	80,81	4,1275	19,58	261,47	26,39	15,00	26,35	9,91	2,66
		Average	**4,58**	**0,32**	**14,66**	**55,34**	**3,19**	**17,29**	**73,53**	**72,71**	**5,00**	**15,28**	**215,67**	**24,52**	**14,20**	**23,45**	**8,69**	**2,70**
		Variance	2,73	0,02	1,88	174,03	0,21	12,09	426,77	335,30	1,34	25,47	4203,23	19,57	0,70	11,47	1,77	0,00
		Standard deviation	1,65	0,13	1,37	13,19	0,45	3,48	20,66	18,31	1,16	5,05	64,83	4,42	0,84	3,39	1,33	0,03
		CV (coeff. of variation)	**0,36**	**0,40**	**0,09**	**0,24**	**0,14**	**0,20**	**0,28**	**0,25**	**0,23**	**0,33**	**0,30**	**0,18**	**0,06**	**0,14**	**0,15**	**0,01**
	Parallel	5 A	4,99	0,3947	12,65	60,71	3,494	17,37	77,64	109,15	4,6771	23,34	260,24	41,38	76,00	16,980	6,29	2,70
		5 B	7,68	0,6763	11,36	56,69	3,494	16,23	77,53	93,32	6,3022	14,81	244,50	36,23	74,00	18,290	6,75	2,71
		5 C	7,70	0,7979	9,65	44,20	3,495	12,65	80,56	60,69	6,3221	9,60	224,62	32,67	77,00	18,700	6,88	2,72
		5 D	14,34	1,1972	11,97	73,75	3,497	21,09	105,93	80,24	3,7471	21,41	234,77	33,43	75,00	19,100	7,02	2,72
		Average	**8,68**	**0,77**	**11,41**	**58,84**	**3,50**	**16,83**	**85,42**	**85,85**	**5,26**	**17,29**	**241,03**	**35,93**	**75,50**	**18,27**	**6,73**	**2,71**
		Variance	15,85	0,11	1,66	148,21	0,00	12,10	188,95	421,02	1,61	39,63	229,86	15,55	1,67	0,85	0,10	0,00
		Standard deviation	3,98	0,33	1,29	12,17	0,00	3,48	13,75	20,52	1,27	6,30	15,16	3,94	1,29	0,92	0,32	0,01
		CV (coeff. of variation)	**0,46**	**0,43**	**0,11**	**0,21**	**0,00**	**0,21**	**0,16**	**0,24**	**0,24**	**0,36**	**0,06**	**0,11**	**0,02**	**0,05**	**0,05**	**0,00**
	Oblique	6 A	6,09	0,4028	15,11	76,26	3,499	21,79	111,66	118,49	4,2076	28,16	303,34	40,69	52,00	20,130	7,46	2,70
		6 B	8,90	0,6389	13,93	88,87	3,499	25,40	111,70	120,51	5,2729	22,85	341,57	62,95	47,00	14,650	5,43	2,70
		6 C	10,24	0,6890	14,86	79,49	3,495	22,75	106,09	106,85	6,3014	16,96	303,37	47,26	65,00	17,330	6,42	2,70
		6 D	9,47	0,7212	13,13	64,79	2,942	22,02	104,77	115,03	5,6816	20,25	290,03	36,83	75,00	21,420	7,88	2,72
		Average	**8,67**	**0,61**	**14,26**	**77,35**	**3,36**	**22,99**	**108,55**	**115,22**	**5,37**	**22,05**	**309,58**	**46,93**	**59,75**	**18,38**	**6,79**	**2,71**
		Variance	3,27	0,02	0,82	98,78	0,08	2,75	13,31	36,23	0,78	22,39	494,40	132,61	160,92	9,11	1,21	0,00
		Standard deviation	1,81	0,14	0,91	9,94	0,28	1,66	3,65	6,02	0,88	4,73	22,24	11,52	12,69	3,02	1,10	0,01
		CV (coeff. of variation)	**0,21**	**0,24**	**0,06**	**0,13**	**0,08**	**0,07**	**0,03**	**0,05**	**0,16**	**0,21**	**0,07**	**0,25**	**0,21**	**0,16**	**0,16**	**0,00**

Table 7: Result overview PPT (2)

			First Failure			3.5 mm				Maximum			Total					
			Load	@ Pen.	SP	Load	@ Pen.	SP	Energy	Load	@ Pen.	SP	Energy	SE	Angle	Mass of De	Volume of Deb	Density
			[kN]	[mm]	[kN/mm]	[kN]	[mm]	[kN/mm]	[J]	[kN]	[mm]	[kN/mm]	[J]	[J/g!!!]	[°]	[g]	[cm³]	[g/cm³]
Granite Gneiss	Normal	7 A	18,96	0,7025	27,00	77,68	3,495	22,23	120,12	207,78	5,9350	35,01	420,58	38,88	0,00	28,45	10,82	2,63
		7 B	18,42	0,5156	35,72	104,80	2,673	39,21	161,09	157,72	5,3066	29,72	538,18	36,54	0,00	38,29	14,73	2,60
		7 C	9,67	0,4082	23,68	79,96	2,529	31,61	100,53	150,86	5,7528	26,22	434,85	46,19	0,00	24,76	9,41	2,63
		7 D	10,13	0,5646	17,95	93,38	3,073	30,38	113,62	98,97	6,2740	15,77	185,69	36,13	0,00	13,26	5,14	2,58
		7 E	16,19	0,7115	22,76	74,20	3,495	21,23	103,49	86,06	3,7106	23,19	223,62	20,48	0,00	28,83	10,92	2,64
		Average	**14,67**	**0,58**	**25,42**	**86,00**	**3,05**	**28,93**	**119,77**	**140,27**	**5,40**	**25,98**	**360,58**	**35,64**	**0,00**	**26,72**	**10,20**	**2,62**
		Variance	20,11	0,02	43,65	163,16	0,20	54,81	595,02	2404,75	1,01	51,88	22501,06	88,19	0,00	81,58	11,90	0,00
		Standard deviation	4,48	0,13	6,61	12,77	0,45	7,40	24,39	49,04	1,00	7,20	150,00	9,39	0,00	9,03	3,45	0,03
		CV (coeff. of variation)	**0,31**	**0,22**	**0,26**	**0,15**	**0,15**	**0,26**	**0,20**	**0,35**	**0,19**	**0,28**	**0,42**	**0,26**	**######**	**0,34**	**0,34**	**0,01**
	Parallel	8 A	15,52	0,6370	24,36	149,33	3,317	45,02	234,46	217,80	5,8127	37,47	626,42	59,22	80,00	27,820	10,58	2,63
		8 B	24,42	0,7880	30,99	144,05	3,006	47,92	216,21	237,31	6,1591	38,53	628,11	55,70	50,00	29,660	11,28	2,63
		8 C	12,45	0,4742	26,25	137,03	3,416	40,12	186,03	146,79	6,2981	23,31	417,96	59,81	82,00	18,450	6,99	2,64
		8 D	16,19	0,6160	26,28	118,90	3,496	34,01	165,39	167,01	6,3059	26,48	494,46	85,16	78,00	15,270	5,81	2,63
		Average	**17,14**	**0,63**	**26,97**	**137,33**	**3,31**	**41,77**	**200,52**	**192,23**	**6,14**	**31,45**	**541,74**	**64,97**	**72,50**	**22,80**	**8,66**	**2,63**
		Variance	26,19	0,02	8,00	176,30	0,05	37,10	947,39	1795,70	0,05	59,11	10729,05	184,48	227,67	49,29	7,16	0,00
		Standard deviation	5,12	0,13	2,83	13,28	0,21	6,09	30,78	42,38	0,23	7,69	103,58	13,58	15,09	7,02	2,68	0,01
		CV (coeff. of variation)	**0,30**	**0,20**	**0,10**	**0,10**	**0,06**	**0,15**	**0,15**	**0,22**	**0,04**	**0,24**	**0,19**	**0,21**	**0,21**	**0,31**	**0,31**	**0,00**
Brixen Granite	Oblique	10 A	13,27	0,5131	25,86	140,24	3,497	40,10	166,02	170,80	6,2992	27,11	462,80	120,83	-	10,150	3,83	2,65
		10 B	17,04	0,6235	27,32	130,64	3,498	37,35	155,59	190,04	5,5335	34,34	576,80	42,87	-	36,060	13,46	2,68
		10 C	10,74	0,4309	24,93	146,10	3,279	44,56	184,37	162,42	6,1119	26,57	507,18	45,20	-	30,070	11,22	2,68
		10 D	16,50	0,6182	26,69	85,98	2,518	34,15	125,99	231,26	5,3324	43,37	589,94	45,95	-	34,280	12,84	2,67
		Average	**14,39**	**0,55**	**26,20**	**125,74**	**3,20**	**39,04**	**157,99**	**188,63**	**5,82**	**32,85**	**534,18**	**63,71**		**27,64**	**10,34**	**2,67**
		Variance	8,67	0,01	1,08	743,24	0,22	19,46	596,75	941,33	0,21	61,72	3583,25	1451,69		142,26	19,70	0,00
		Standard deviation	2,94	0,09	1,04	27,26	0,47	4,41	24,43	30,68	0,46	7,86	59,86	38,10		11,93	4,44	0,01
		CV (coeff. of variation)	**0,20**	**0,17**	**0,04**	**0,22**	**0,15**	**0,11**	**0,15**	**0,16**	**0,08**	**0,24**	**0,11**	**0,60**		**0,43**	**0,43**	**0,01**

Table 8: Result overview PPT (3)

			First Failure			3.5 mm				Maximum			Total					
			Load	@ Pen.	SP	Load	@ Pen.	SP	Energy	Load	@ Pen.	SP	Energy	SE	Angle	Mass of De	Volume of Deb	Density
			[kN]	[mm]	[kN/mm]	[kN]	[mm]	[kN/mm]	[J]	[kN]	[mm]	[kN/mm]	[J]	[J/g!!!]	[°]	[g]	[cm³]	[g/cm³]
Imberg Sandstone		11 A.1	9,54	0,7217	13,22	82,05	3,499	23,45	107,17	130,41	4,9043	26,59	399,37	32,48	-	31,35	12,29	2,55
		11 A.2	16,63	1,0413	15,97	95,81	3,495	27,41	120,68	169,19	6,3011	26,85	398,13	64,87	-	15,65	6,14	2,55
		11 A.3	12,20	0,8755	13,93	104,54	3,493	29,93	125,66	145,49	6,2929	23,12	344,84	78,44	-	11,21	4,40	2,55
		Average	**12,79**	**0,88**	**14,38**	**94,14**	**3,50**	**26,93**	**117,84**	**148,36**	**5,83**	**25,52**	**380,78**	**58,60**		**19,40**	**7,61**	**2,55**
		Variance	12,82	0,03	2,03	128,58	0,00	10,68	91,46	382,16	0,65	4,34	969,14	557,52		111,97	17,22	0,00
		Standard deviation	3,58	0,16	1,43	11,34	0,00	3,27	9,56	19,55	0,80	2,08	31,13	23,61		10,58	4,15	0,00
		CV (coeff. of variation)	**0,28**	**0,18**	**0,10**	**0,12**	**0,00**	**0,12**	**0,08**	**0,13**	**0,14**	**0,08**	**0,08**	**0,40**		**0,55**	**0,55**	**0,00**
		11 B.1	15,39	1,1106	13,86	70,92	3,495	20,29	88,60	167,66	5,2526	31,92	382,37	38,22	-	25,51	10,00	2,55
		11 B.2	13,90	0,9694	14,34	78,25	3,499	22,36	103,56	169,64	5,1002	33,26	437,04	36,87	-	30,23	11,85	2,55
		11 B.3	28,38	1,7080	16,61	87,41	3,495	25,01	109,67	139,04	4,8835	28,47	414,38	63,79	-	16,50	6,50	2,54
		Average	**19,22**	**1,26**	**14,94**	**78,86**	**3,50**	**22,55**	**100,61**	**158,78**	**5,08**	**31,22**	**411,26**	**46,29**		**24,08**	**9,45**	**2,55**
		Variance	63,41	0,15	2,17	68,25	0,00	5,60	117,48	293,08	0,03	6,10	754,49	230,08		48,66	7,41	0,00
		Standard deviation	7,96	0,39	1,47	8,26	0,00	2,37	10,84	17,12	0,19	2,47	27,47	15,17		6,98	2,72	0,01
		CV (coeff. of variation)	**0,41**	**0,31**	**0,10**	**0,10**	**0,00**	**0,10**	**0,11**	**0,11**	**0,04**	**0,08**	**0,07**	**0,33**		**0,29**	**0,29**	**0,00**
			16,01		14,66					153,57		28,37	396,02					
	without confinement	11 C.1	10,12	0,8658	11,69	=MAX				22,54	1,5779	14,28			-		0,00	2,55
		11 C.2	20,56	1,2949	15,88	=MAX				20,56	1,2949	15,88			-		0,00	2,55
		11 C.3	11,60	0,8276	14,02	=MAX				22,97	1,5255	15,05			-		0,00	2,55
		11 C.4	12,71	0,9550	13,31	=MAX				19,97	1,3663	14,62			-		0,00	2,55
		Average	**13,75**	**0,99**	**13,73**	**#DIV/0!**	**#DIV/0!**	**#DIV/0!**	**#DIV/0!**	**21,51**	**1,44**	**14,96**	**#DIV/0!**	**#DIV/0!**				
		Variance	21,75	0,05	3,01	#DIV/0!	#DIV/0!	#DIV/0!	#DIV/0!	2,14	0,02	0,48	#DIV/0!	#DIV/0!				
		Standard deviation	4,66	0,21	1,73	#DIV/0!	#DIV/0!	#DIV/0!	#DIV/0!	1,46	0,13	0,69	#DIV/0!	#DIV/0!				
		CV (coeff. of variation)	**0,34**	**0,22**	**0,13**	**#DIV/0!**	**#DIV/0!**	**#DIV/0!**	**#DIV/0!**	**0,07**	**0,09**	**0,05**	**#DIV/0!**	**#DIV/0!**				

Table 9: Result overview PPT (4)

			First Failure			3.5 mm				Maximum			Total					
			Load	@ Pen.	SP	Load	@ Pen.	SP	Energy	Load	@ Pen.	SP	Energy	SE	Angle	Mass of De	Volume of Deb	Density
			[kN]	[mm]	[kN/mm]	[kN]	[mm]	[kN/mm]	[J]	[kN]	[mm]	[kN/mm]	[J]	[J/g!!!]	[°]	[g]	[cm³]	[g/cm³]
Schist Gneiss	Oblique	12 A	5,36	0,5471	9,80	45,77	2,959	15,47	71,22	68,29	4,7120	14,49	187,75	22,92	40,00	23,750	8,19	2,90
		12 B	6,07	0,3842	15,81	53,44	3,495	15,29	84,02	90,12	5,3321	16,90	271,61	101,77	46,00	7,740	2,67	2,90
		12 C	7,31	0,3592	20,36	83,60	3,498	23,90	92,69	103,39	4,4064	23,46	264,28	29,94	37,00	25,690	8,83	2,91
		12 D	8,97	0,3958	22,67	78,46	3,025	25,94	94,28	122,60	5,0606	24,23	353,66	75,01	40,00	13,720	4,71	2,91
		Average	**6,93**	**0,42**	**17,16**	**65,32**	**3,24**	**20,15**	**85,55**	**96,10**	**4,88**	**19,77**	**269,32**	**57,41**	**40,75**	**17,73**	**6,10**	**2,91**
		Variance	2,50	0,01	32,17	343,35	0,09	31,03	111,62	521,45	0,16	23,19	4599,50	1407,11	14,25	71,83	8,50	0,00
		Standard deviation	1,58	0,09	5,67	18,53	0,29	5,57	10,56	22,84	0,40	4,82	67,82	37,51	3,77	8,48	2,92	0,01
		CV (coeff. of variation)	**0,23**	**0,20**	**0,33**	**0,28**	**0,09**	**0,28**	**0,12**	**0,24**	**0,08**	**0,24**	**0,25**	**0,65**	**0,09**	**0,48**	**0,48**	**0,00**
Overall CV (coefficient of variation)			**0,25**	**0,21**	**0,12**	**0,18**	**0,10**	**0,16**	**0,16**	**0,17**	**0,13**	**0,22**	**0,15**	**0,30**		**0,30**	**0,30**	

Table 10: Result overview PPT (5)

The below load-penetration diagrams (Figure 24 and Figure 25) show the same result as the calculation of the variation coefficients, but even more obvious. The diagram for the first failure point (Figure 24) reveals a strong correlation between the penetration and the force at which the first failure occurred with numbers of the coefficient of determination between 35,7% and 99,7%. On the other hand there is nearly no correlation between the force and the penetration for the points where the maximum force was measured. For those regression lines the coefficient of determination is between 0,4% and 80,0% (Figure 25).

This means, that there is a strong correlation for the point where the first chipping is monitored, but there is nearly no more interrelationship for measured points or failure events later on during the test.

The outcome of this study is that the specific penetration for the first failure point is the most consistent parameter that can be determined for the punch penetration test. The first failure point is also free of systematic errors and within the best range while conducting the test for characterizing the initiation and the chipping process itself.

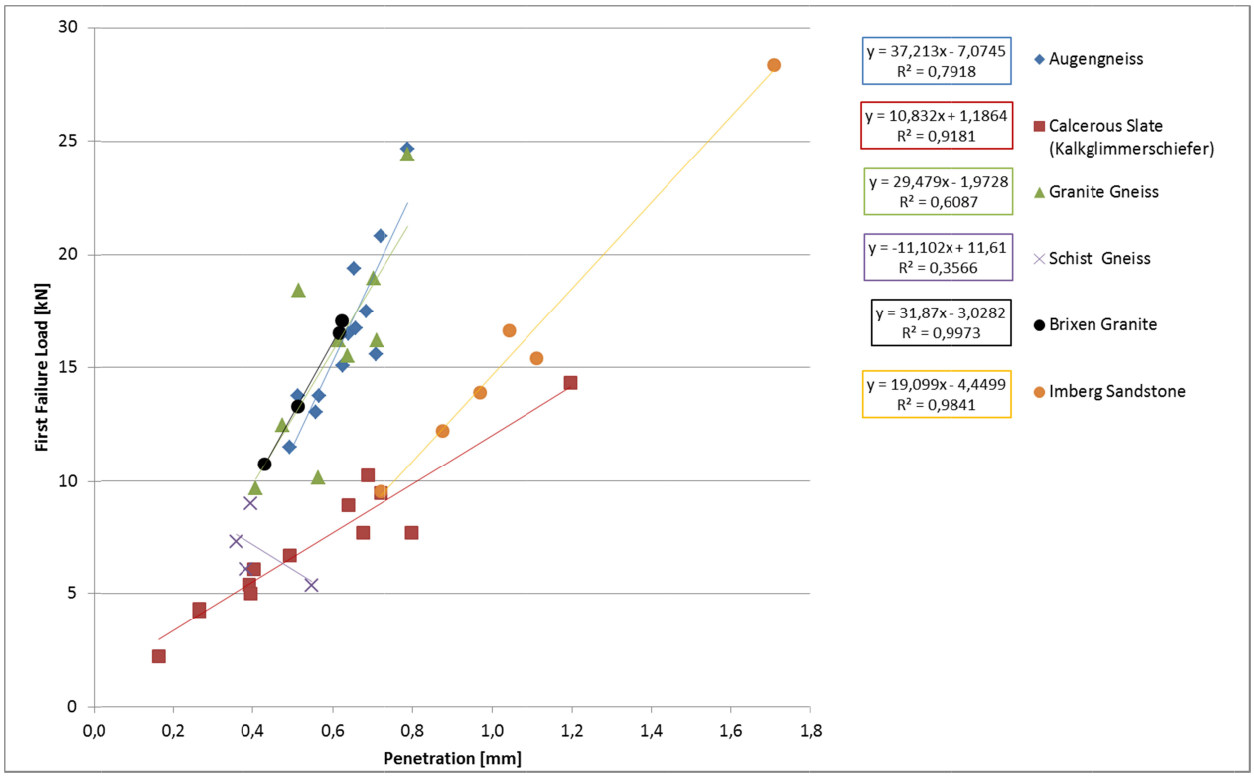

Figure 24: First Failure SP

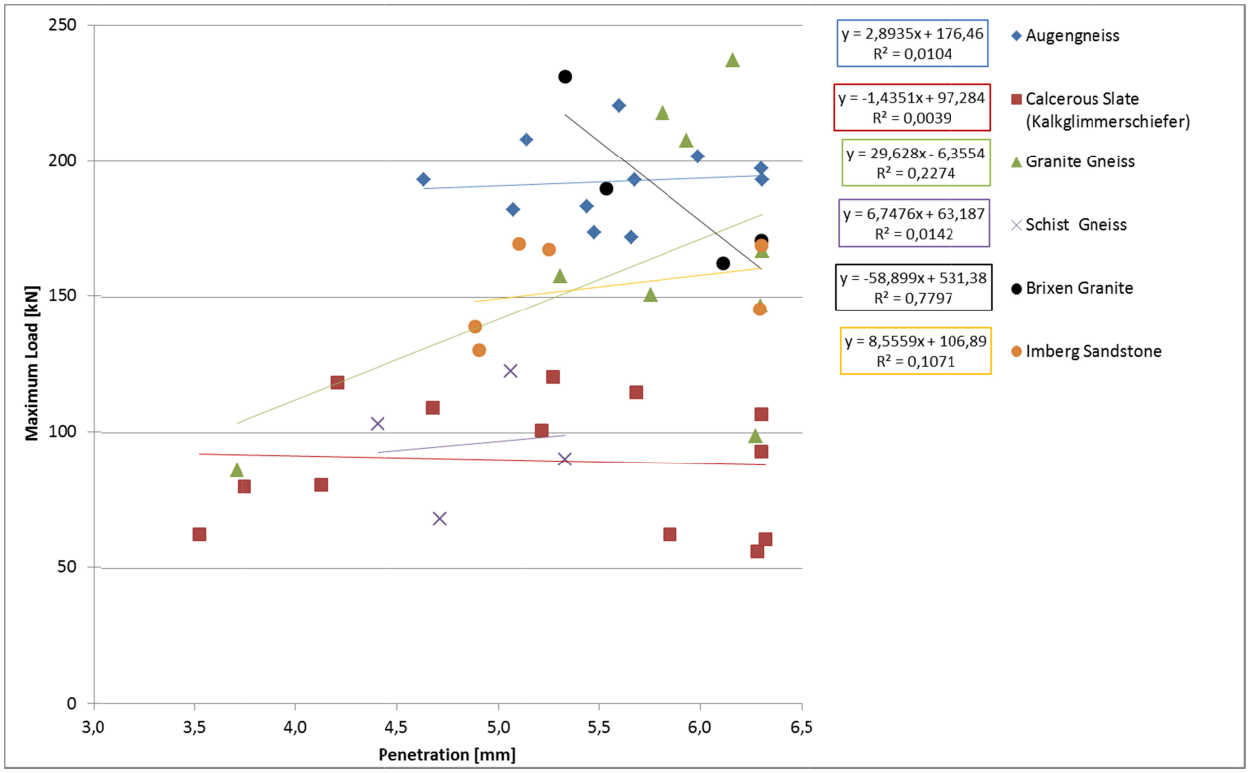

Figure 25: Maximum SP

Evaluation of the graphs: brittle vs. ductile rocks

The force – penetration graph and its gradient is an indicator for the excavatability of the rock and also for the required energy input for efficient chipping, but there are also some other interesting things, that can be obtained by having a closer look at the pictures.

The graph is also an indicator for rock brittleness. If the chart shows a highly fluctuating relationship between force and penetration, because of the creation of chips, we will assume that this is a brittle rock.

In less brittle or ductile rocks, the curves are smoother and there are not any sudden force drops in the graph.

The two graphs below (Figure 26 and Figure 27) show the comparison of a highly brittle rock (Augen Gneiss) with a very ductile rock (Schist Gneiss). The difference in the course of the curve is obvious. Each peak in the top diagram stands for a failure event where possibly a chip emerged. Such events are always accompanied by loud noises.

On the other hand stands the bottom diagram which does not show any sharp tips at all and does not produce any noises during the test.

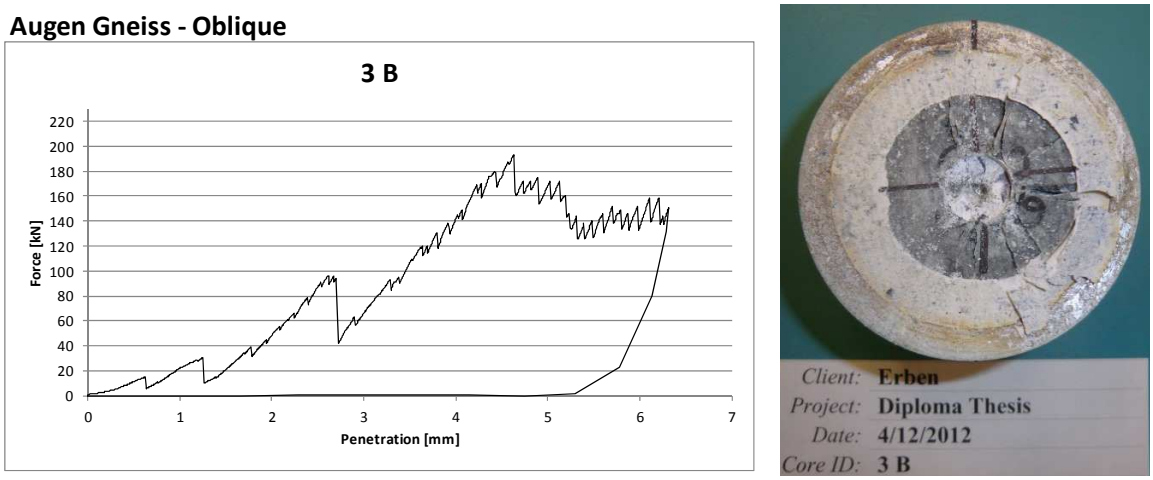

Figure 26: Force-penetration graph of a brittle rock

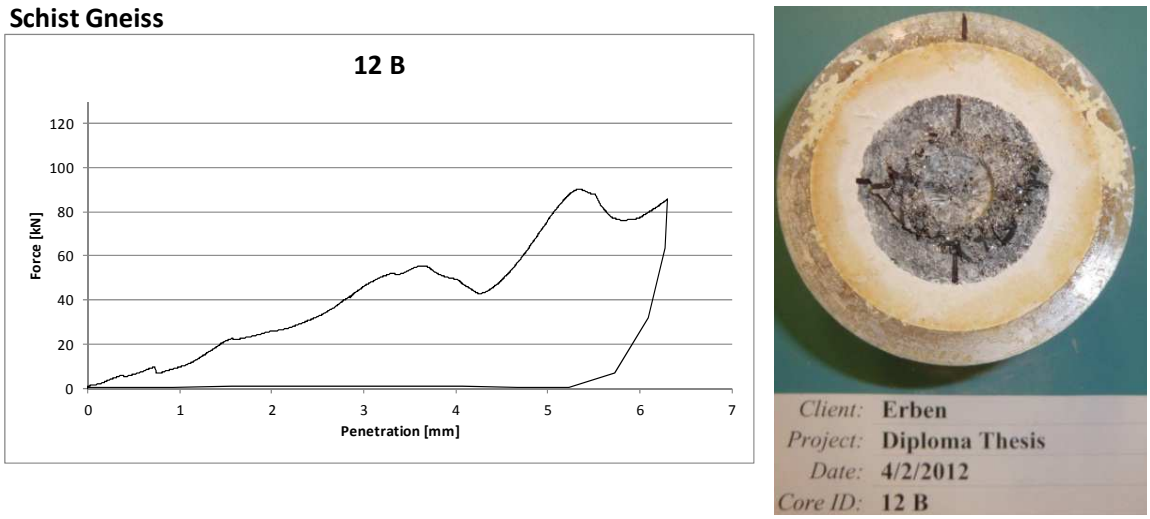

Figure 27: Force-penetration graph of a ductile rock

2.2.3 Correlation of the PPT with geotechnical standard tests (UCS, BTS) and LCM tests

A topic that is examined very shortly, is the relationship between the results obtained from punch penetration tests and two geotechnical standard tests, the UCS and the BTS. For this thesis the data sets of two independent studies were used. One set comes from Gertsch's dissertation *[7]* and the second from the tests conducted during this research. Gertsch's data was used because of the complete data sets needed for the comparison. The testing equipment Gertsch used, was in general the same that was used during this study with a few changes:

The first thing is that he used a hemispherical indenter and now a conical shaped indenter was used. The second change is the way the samples are confined at their bottom, but this will not affect the results in any way. The third improvement is the data acquisition system that is being used nowadays. The temporal resolution of the measuring channels has improved a lot and therefore it is possible to find points of first failure which would never have been detected ten years ago.

As it can be seen in the diagrams (Figure 28), the connection between the specific penetration for the point of first fracture (FF SP) and the UCS with a coefficient of determination of 71% and 56% cannot be neglected.

For the correlation between BTS and PPT FF SP the results between Gertsch's data and the actual data diverge widely.

One thing that leaps to the eye when looking at the figures and needs to be mentioned is the immense difference of the numeric value regarding the specific penetration level between these two studies. SP in Gertsch's examination ranged from 24 to 206 kN/mm whereas SP in the actual study ranges from 12 to 27 kN/mm. This circumstance is hard to explain as some of the lithologies covered the same rock strengths.

To verify and check the plausibility of either data, the results of Cigla's dissertation were compared to the actual data *[26]*. Cigla did not give complete data sets for his PPT, but he listed the PSI for all his tests, which were compared to the PSIs of the actual study. The PSI is, as already mentioned, nothing more than the specific penetration for the point where the maximum load is measured throughout the test and the corresponding penetration.

Ciglas PSI ranged from 15 to 38 kN/mm and the PSI of this research ranged from 15 to 35 kN/mm. One of Ciglas lithologies, the Colorado Red Granite was also used by

Gertsch. Cigla measured a PSI of 37 kN/mm and Gertsch a PSI of 206 kN/mm for the same rock type!

To sum up the realizings of this comparison it is hard to trust Gertsch's data anymore, because of the huge difference between his values and the values presented by other studies. The results of this actual research correspond pretty well with other studies and pass a plausibility check.

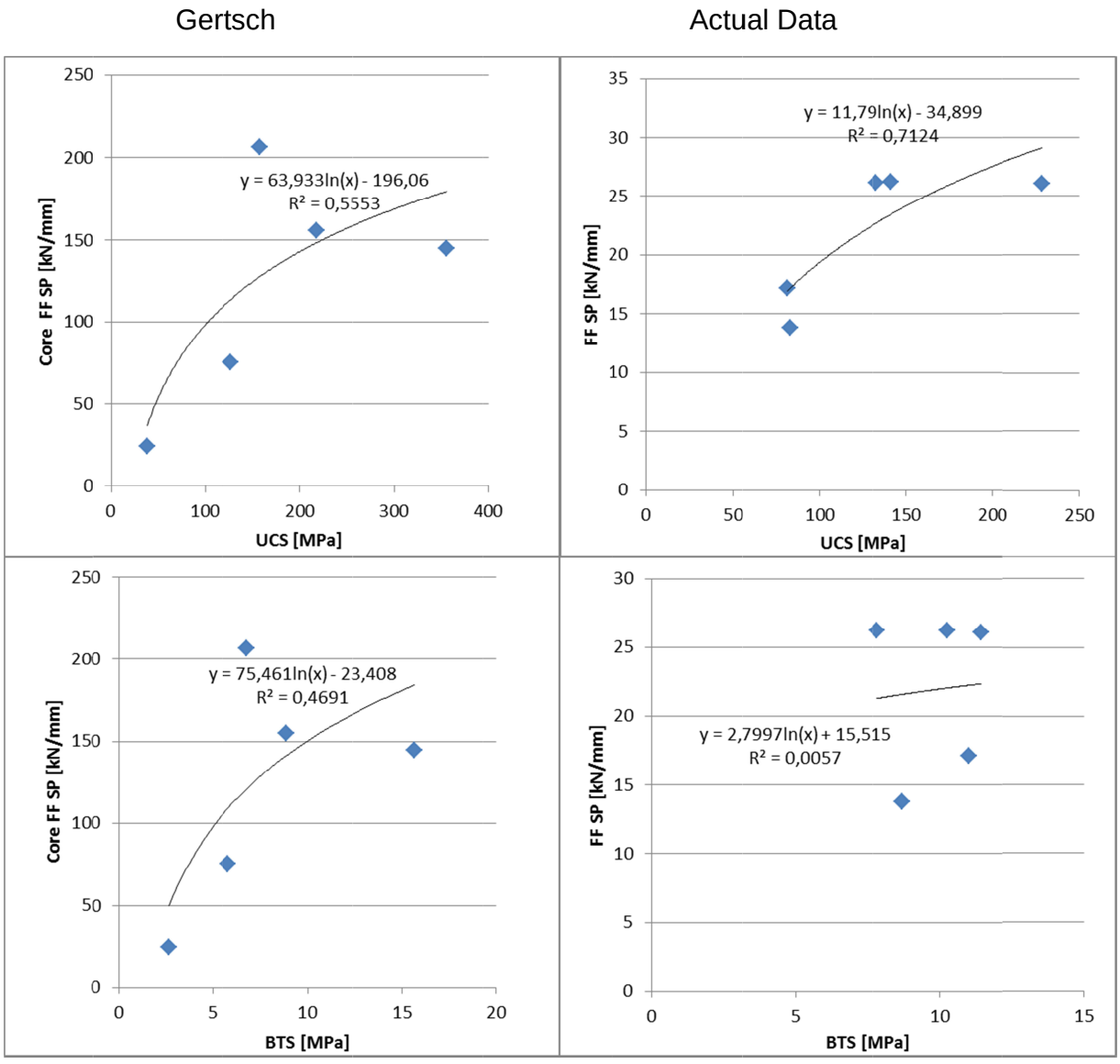

Figure 28: Correlation of the PPT with UCS and BTS tests with Gertsch's and the actual data

To correlate the results of the PPT with the specific penetration of the linear cutting tests seems useless when one looks at the scattered points in Figure 29. This does not necessarily mean that the PPT is not suitable for predicting the cutting forces, because for predicting them a lot of geometrical parameters are considered.

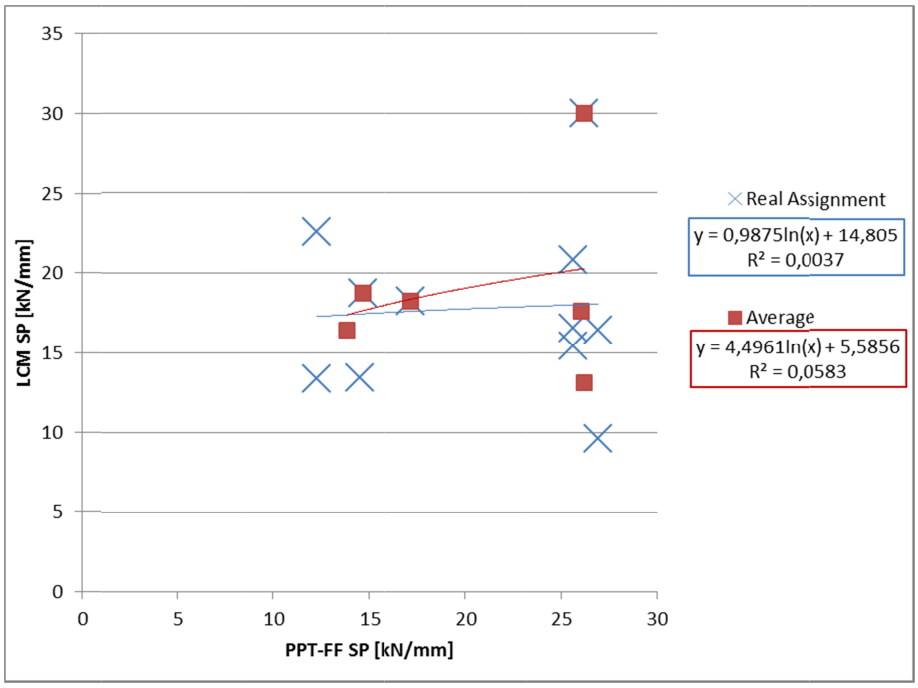

Figure 29: Correlation between linear cutting tests and PPT

2.2.4 Influence of foliation/ planes of weakness on the results of the PPT

The influence of the direction of foliation on the results of the PPT is hard to tell out of this study. First of all the problem is, that within this study the requirement to have foliation angles in the range between 0 and 90 degrees was just fulfilled by two lithologies, the Calcareous Mica Schist and the Granite Gneiss.

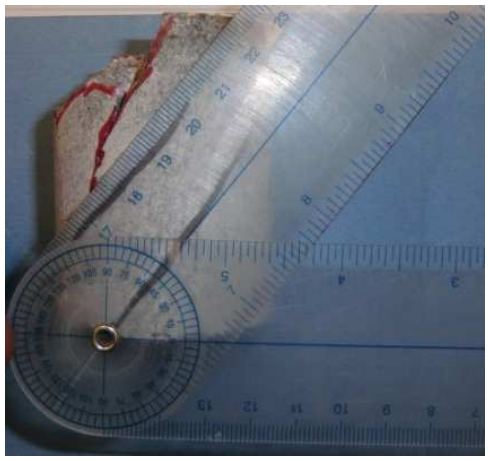

For the two other lithologies with a clearly observable foliation the range of investigated dip angles was just between 35 and 63 degrees for the Augen Gneiss and between 37 and 46 degrees for the Schist Gneiss. These small ranges just lead to point clouds

when illustrated as it can be observed in the diagram.

However, the two lithologies that meet the requirements show a correlation, although it is weak, between the angle of foliation and the examined parameters such as the specific penetration for the first failure point, the penetration at the FF (Figure 31) and the energy (Figure 32). Especially the Calcareous Mica Schist is worth mentioning.

One of the most interesting observations is that with an increasing angle of foliation the penetration depth at which the first failure occurs, rises and so does the load.

This notice can be explained by the simple fact, that a rock surface, or any surface in general, fails earlier with increasing brittleness of the material and the more the load is applied in an angle normal to the schistosity.

In contrast, if the direction of loading is parallel to the direction of foliation, the indenter penetrates the rock by moving into it in-between two schistosity planes without immediately causing a major failure.

The second thing that can be observed is that with an ascending dip angle the energy consumption for the test increases as well. This can be explained by the less efficient chipping process that happens to samples where the foliation is parallel to the penetration direction of the indenter. Cleaving of the rock obviously consumes more energy and creates less and later chipping. This leads to less free surfaces where the rock can avoid the load of the indenter and the energy consumption increases.

After these tests it is too early to talk about a distinctive anisotropy of the PPT, which is definitely existent. A lot more tests with a dip angle between 0 and 90 degrees need to be carried out for the other lithologies to base the theory on more data.

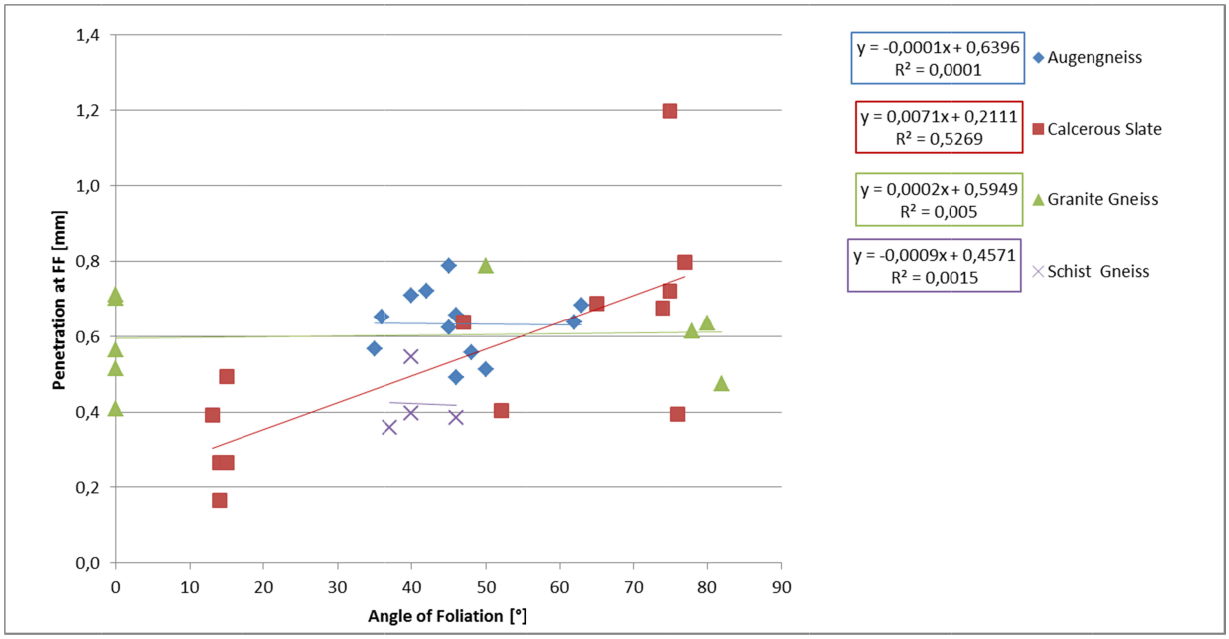

Figure 31: Correlation between angle of foliation and penetration at the first failure point

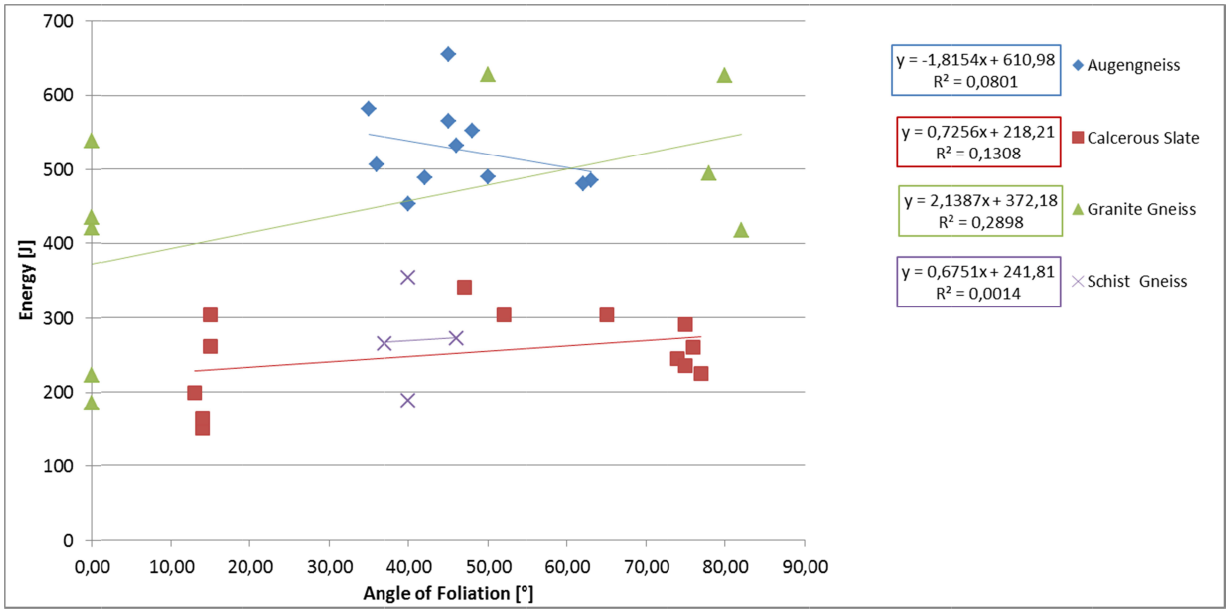

Figure 32: Correlation between angle of foliation and consumed energy

2.2.5 Failure Mechanism – Fracture Analysis

There are three steps that need to be done when analyzing the failure process of the rock core after the punch penetration test.

The first step is to take pictures of the top side of the rock cylinder before and after the test. After executing the test it is already possible to see from the left crater and the created chips whether the rock is rather brittle or ductile. The pictures ensure that it is still possible to analyze the chip size and crack pattern even after removing the chips for further investigations. There are several remarkable things that can be observed when describing the sample surface after the test.

To make sure that the indenter is placed exactly in the center of the rock core for each test, a ninety degree cross marked the right spot on the rock. What was interesting was that the center of the cross was still in place after the test, but the width of the lines was enlarged due to the indentation. The enlargement can simply be explained by the fact that the surface of the material is growing from the area of a circle to the surface area of a cone during the indentation process. The clarity of this mechanism is more distinct the more porous the rock is. Figure 33 shows an Imberg sandstone sample where this behavior is very notable.

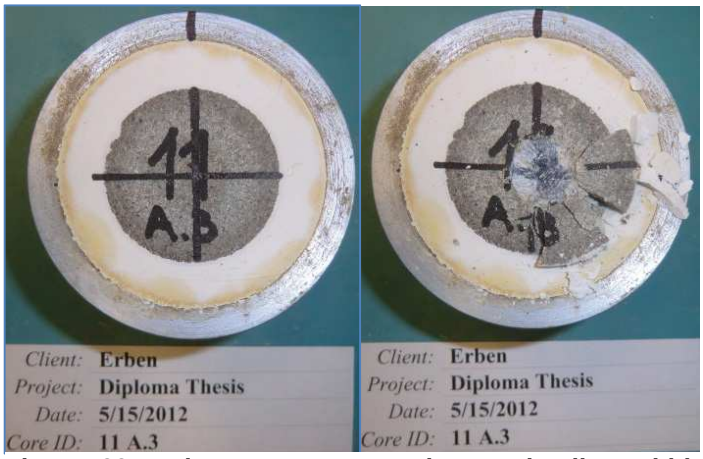

Figure 33: Indenter pressure enlarges the line width (Imberg Sandstone)

Another thing that would be expected and is also verified by tests is the effect of the foliation of

Figure 34: Failure along schistosity planes (Augen Gneiss)

the sample on the failure direction of the rock. As it can be clearly seen in Figure 34 where the dip direction is indicated by the red arrow the top part of the rock sample fails in direction of the schistosity. The failure along planes of weakness is very distinctive and can easily be noticed on lithologies that are referred to as “oblique”. This means they have a dip angle between 30 and 60 degrees such as the Augengneiss in the picture.

Further discussion on the results of the foliation on the failure process will be led in step two of the analysis.

The difference in the failure mode of the top of the rock core between brittle and ductile rock is obvious when you compare the surface of the sample in Figure 35 with the surface in Figure 36.

Ductile rocks do not fail suddenly and do not tend to form large chips as brittle rocks do. As mentioned before the force-penetration graphs for the ductile lithologies look very smooth. This explains why no noises are occurring while testing.

When looking on top of the sample after conducting the test there are not any pieces of rock missing, but the rock was simply displaced by the indenter and moved to the side where it procrastinated. After removing the debris from around the crater one can clearly see the primary crushed zone in the very right picture of Figure 35: Ductile rock (Schist Gneiss)Figure 35. Around this crushed zone pieces of rock are missing. They were pushed away by the indenterwhile material was coming from the center, where the indenter pushed down and needed space.

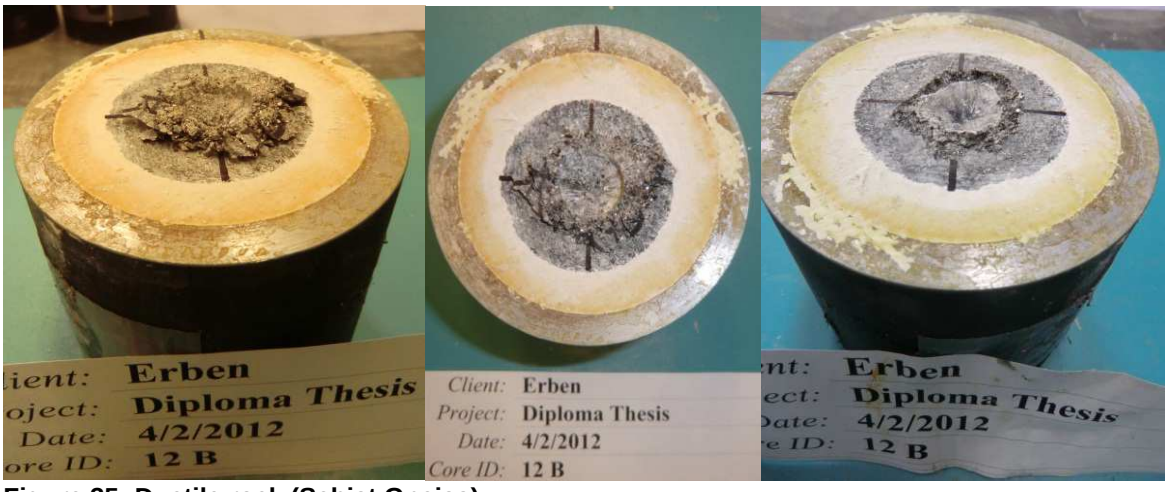

Figure 35: Ductile rock (Schist Gneiss)

On the other hand are brittle rocks that fail very suddenly and whose force-penetration graphs show very sharp spikes. During such a failure, that is marked by a tip in the graph and usually accompied by the creation of a chip, a loud noise occurs. After the test the created chips are usually still on top of the sample, although they are not in place anymore.

As can be seen in Figure 36 brittle rocks tend to form large, wedge shaped chips with a depth of about 3 to 10 mm at the edge to the Hydrostone. In the right picture of Figure 36 it is clear to see how deep the chips reach and how they destroy the Hydrostone. A closer look at this picture shows, that there is a ring formed around the rock core with the deepest areas at the transition from rock to Hydrostone. This is because this is the easiest way for the system to fail and release energy with the steel ring on the outside:

The rock chips press against the Hydrostone and start breaking the cement apart. The Hydrostone now tries to find the easiest way to evade the load and this is by failing to the free surface, because of the high strength of the steel ring.

Figure 36: Brittle rock (Augen Gneiss)

When taking the debris away one of the first things that catches attention is the primary crushed zone of compacted material which emerges directly under the indenter. It is formed by crushing the rock and a recompaction of the same material under the load of the indenter. This means that the primary zone is sometimes removable as an intact uniform object but sometimes it is inseparably connected with the secondary crushed zone lying directly underneath. The length,width and depth of the primary crushed zone depends on the rock type and the dip angle, but it is always close to the shape of a hemisphere and with a thickness of 2 to 5 mm.

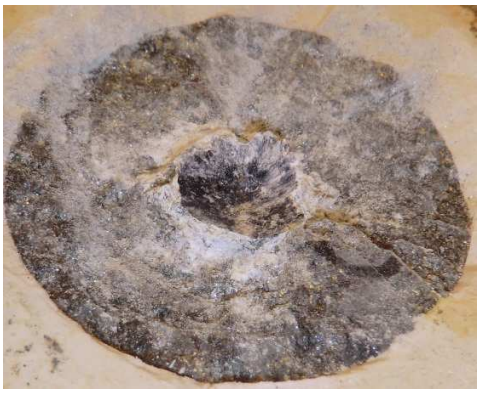

Figure 38: PCZ in place (Calcareous Mica Schist, 4B)

Figure 38: Primary crushed zone (Imberg

The second step to analyze the failure mechanism on the lateral surfaces of the rock cores is to get the Hydrostone and the rock cores, which are still confined by the cement, out of the steel rings. This is done by a hydraulic ram which presses the Hydrostone cylinder out of the rings. To see the way the rock failed on the outside it is necessary to remove the Hydrostone (Figure 39). As the Hydrostone is very brittle, it is easy to crack it into two parts and take the rock core out which is usually not connected to the Hydrostone, because of its smooth surface.

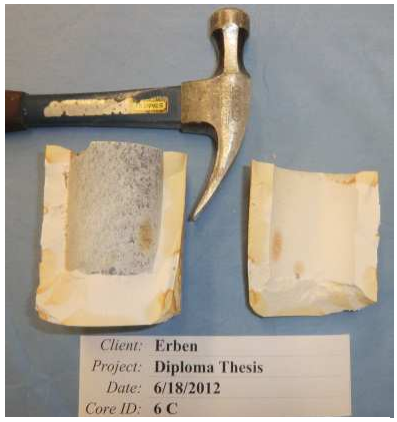

Figure 39: Breaking the Hydrostone with a geologist's hammer

After that all the existing cracks on the rock core are traced with a red permanent marker to make sure that after cracking the core into two parts (step 3) original cracks are still distinguishable from cracks that were induced during the opening process.

Figure 40 shows how each existing crack on each „unwrapped“ rock sample was carefully marked with a red permanent marker and documented with pictures. The black lines illustrate the dip angle of the schistosity and the black arrows on the top surface of the rock cores show the direction of dipping.

Figure 40 and Figure 41 describe the considerable effect of the direction of foliation on the direction of failure and fissures. Especially the upper part of the rock core is pervaded by cracks parallel to the foliation, that meet each other and lead to loose rock parts after the Hydrostone has been removed.

For all oblique lithologies the outer top part of the sample in direction of the foliation is completely seperated. Even for lithologies with a very shallow dip angle, such as the Calcareous Mica Schist (4C) in Figure 41 with a dip angle of 15 degrees, this

observation is true. The reason are lateral cracks which can easily „travel“ along those natural planes of weakness in the rock, and lead to large, loose fragments of rock just held in place during the test by the Hydrostone.

The more horizontal the foliation is, the larger the part of the cylinder top where the rock pieces are completely separated from the core becomes. The uppermost part of isotropic, homogenous rocks such as the Brixen Granite and the Imberg sandstone, tends to fail like it does on rocks with a horizontal foliation, where simply a disc of chips with a height of 5 to 10 mm is sectioned.

However the difference in the texture of the surface after removing the debris is obvious. The surface of homogenous rocks is very rough and abrasive whereas the top of rocks with a horizontal foliation is smooth because of the failure along schistosity planes, which are generally plainer.

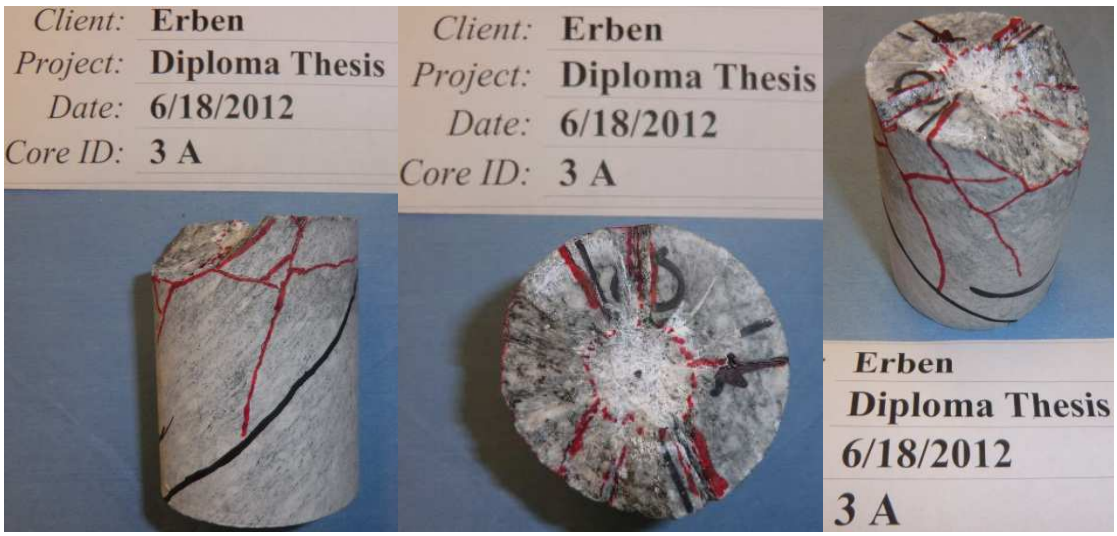

Figure 40: Marking of existing cracks (Augen Gneiss)

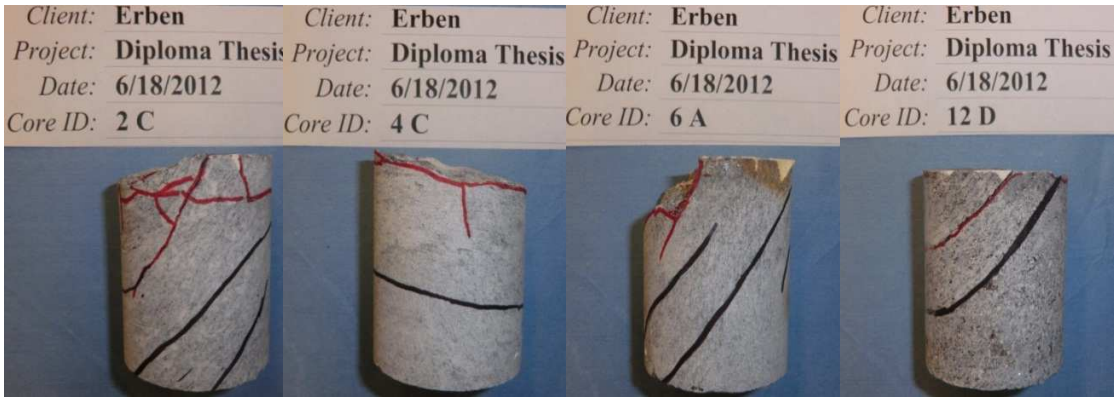

Figure 41: Failure cracks along schistosity: Augen Gneiss (2); Calcareous Mica Schist (4, 6); Schist Gneiss (12)

After observing the side of the rock cores a view of the top reveals some more interesting facts based on the influence of foliation on the failure mechanism.

Following the removal of the debris, the larger fragments that were hold in place by the confining Hydrostone and the primary crushed zone (PCZ), the secondary crushed zone (SCZ) comes into the open. The consistency of this zone is different from the primary: It is less packed, granular and although the minerals are already partly crushed, you can still distinguish the different minerals. Another thing that differentiates it clearly from the primary crushed zone is the fact that it is still together with the rock core as one unit.

Figure 42 and Figure 43 show oblique lithologies with a dip angle between 40 and 80 degrees. The thing that leaps into the eye is that for these rocks the shape of the SCZ differs considerably from a circular shape as it can be seen in Figure 44. Figure 44 depicts rocks with a horizontal schistosity (Calcareous Mica Schist – 4 and Granite Gneiss 7) and with no foliation at all (Brixner granite – 10). For a horizontal foliation and a homogenous, isotropic rock the secondary crushed zone is always of circular shape.

Especially the shapes of the SCZ of the oblique Augen Gneiss with a foliation angle of 50 degrees and the Schist Gneiss (40 degrees) look more like an ellipse than a circle.

Another thing that is worth mentioning is the shift of the center of the secondary crushed zone in the direction of dip as it can be seen in Figure 42 for the Calcareous Mica Schist (5, 6). Further discussion on this phenomenon will be lead in step 3, where the rock cores are sectioned and the extensions of the secondary crushed zone can be clearly seen.

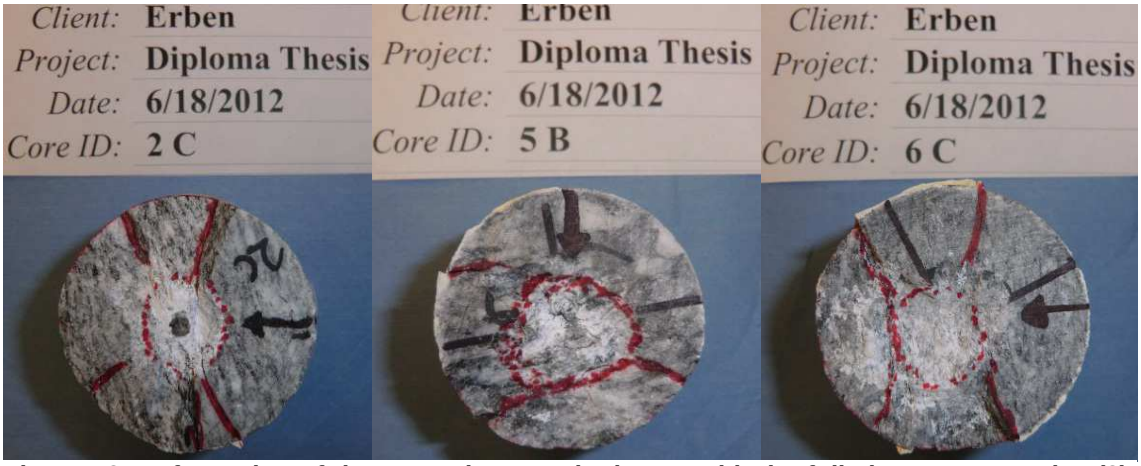

Figure 42: Deformation of the secondary crushed zone with the foliation: Augengneiss (2); Calcareous Mica Schist (5, 6)

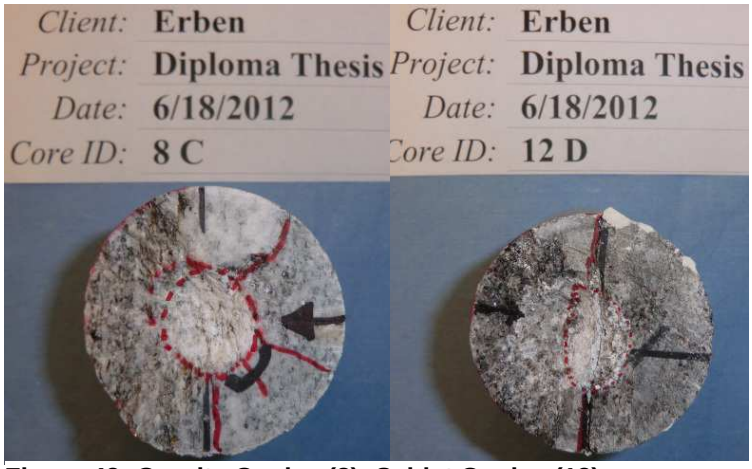

Figure 43: Granite Gneiss (8); Schist Gneiss (12)

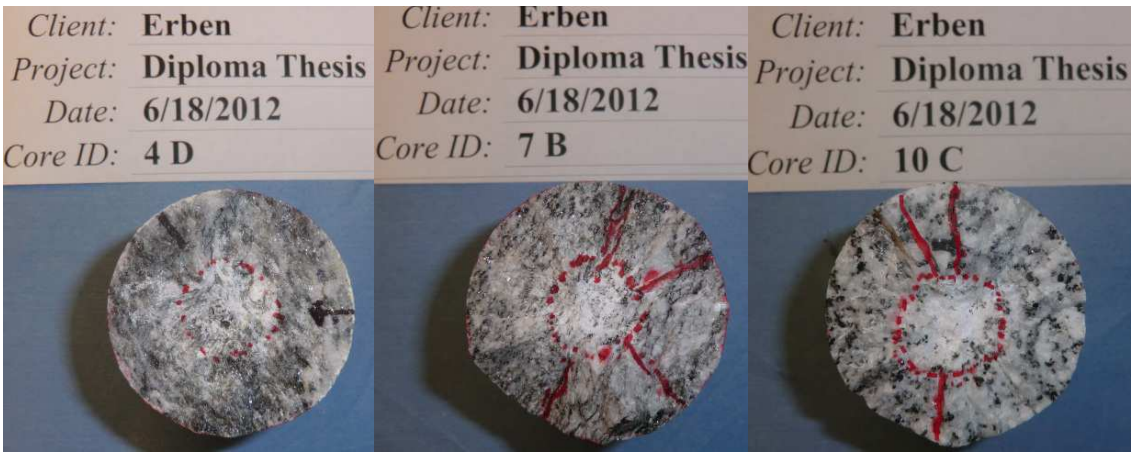

Figure 44: Calcareous Mica Schist (4); Granite Gneiss (7); Brixen Granite (10)

Another thing that is special for brittle, homogenous, isotropic rocks under the load of an indenter is that they tend to split nearly perfect into completely equal halves or quarters. Figure 46 displays the existing cracks on the rock cores after testing. In the top view you can see cracks radiating out from the center with an angle of 90 degrees in-between. In the side view it is obvious that those cracks are running straight down the side of the sample. The reason why the rock core is not already split is the confinement that has been removed and the fact that the penetration of 6,35 mm was still too little.

The lithologies with a clear foliation show this behavior to split apart as well, but the cracks are always following the schistosity, and in most cases only two parts with no geometrical similarity at all develop, as it can be witnessed in Figure 40.

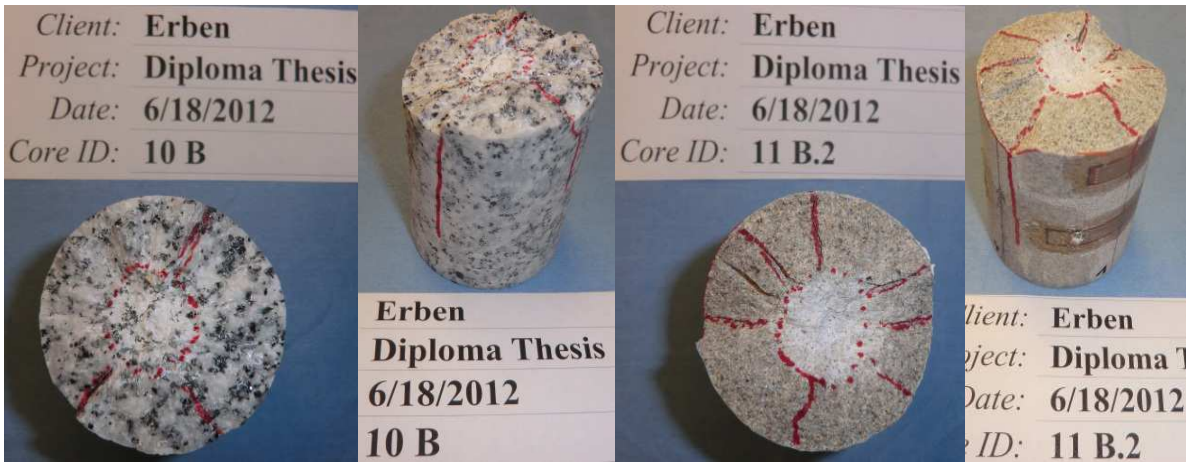

Figure 46: Homogenous rocks tend to split into halves/quarters (Brixen Granite - 10; Imberg Sandstone - 11)

Figure 45: All samples before "unwrapping"

The third and last step is to break the rock core along an existing crack, which occurred during the test and was existent on every core, into two parts. By doing this it is possible to see what happened directly under the indenter and to analyze the different failure zones that developed during the loading.

The most interesting things that the split samples reveal are a cross section through the secondary failure zone and pattern of lateral cracks radiating out from the crushed zone.

Median cracks are very rare to observe on the split samples, because on most rock cores there is only one vent crack and this one is used for splitting them. This can be seen by the red color in the pictures when having a closer look at the edges of the split sample which comes from the marked cracks.

The first thing to talk about is the secondary crushed zone, which consists of crushed, but still granular material so that in most cases even the single minerals can be detected. The border between the SCZ to the “intact” rock is very sharp and can therefore clearly be marked. The SCZ has the shape of an onion, which grows larger in depth and comes to a quite abrupt end. Although the diameter of the indenter is just 19 mm, the width of the crushed zone can reach up to 26 mm. This means that the SCZ grows with increasing depth and distance from the indenter in width. The reason for this is the way stress spreads out under the load of the indenter. Basic research has shown that stress trajectories under a point load have the same onion shape as the SCZ has in Figure 48 and Figure 47.

Figure 48: Growth of the SCZ with depth: Augen Gneiss (3); Calcareous Mica Schist (6)

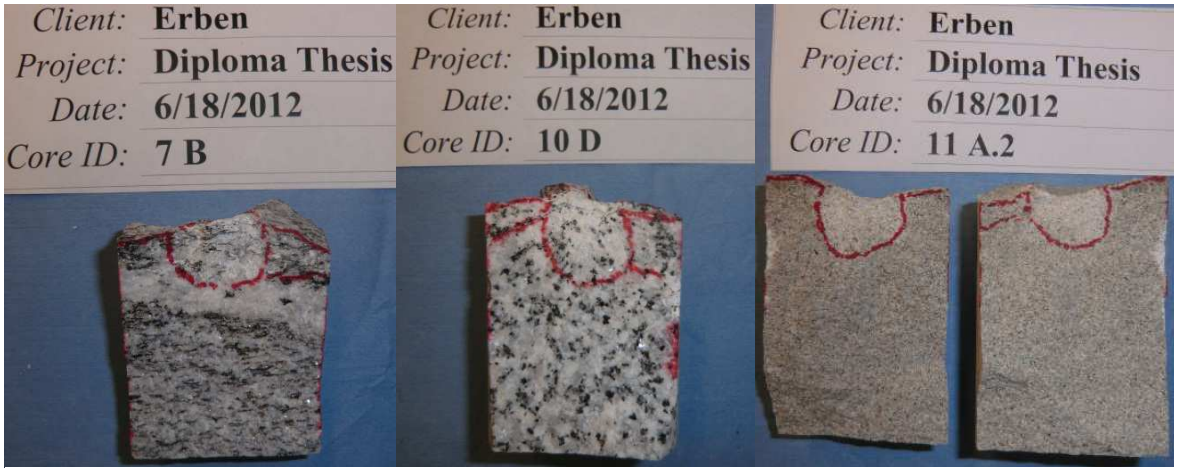

Figure 47: Growth of the SCZ with depth: Granite Gneiss (7); Brixen Granite (10); Imberg sandstone (11)

Although the crushed zone extends with increasing depth, there are many factors its shape depends on.

First of all is the shape of the SCZ dependent on the type of rock. Ductile rocks generally tend to exhibit shallower, but wider crushed zones (Figure 49) than brittle rocks do (Figure 47). This is due to the fact that ductile rocks fail in a more controlled way under the load of the indenter with the stress radiating more to the side and the lesser ability to conduct the forces into depth.

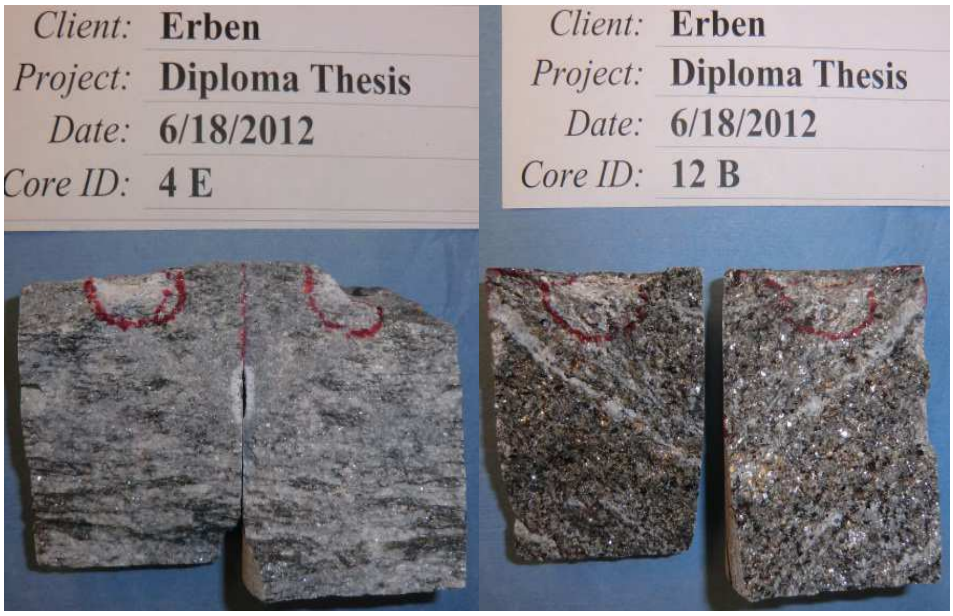

Figure 49: Shallower secondary crushed zone in ductile rocks: Calcareous Mica Schist (4); Schist Gneiss (12)

Another parameter that can lead to a shallower SCZ is a horizontal schistosity. This also prevents the stresses from getting deep into the rock.

The direction of foliation in relation to the direction of loading generally plays a major role in the shape of the crushed zone. Figure 50 shows the connection between the schistosity and the propagation of the SCZ. Especially in the right picture the crushed zone is obviously following the foliation. In the left picture it is a little more difficult to perceive, because of the big fragment missing in the top part, which is absent as a result of failure in orientation of the foliation.

Figure 50: Propagation of the SCZ in direction of foliation: Augen Gneiss (3); Granite Gneiss (8)

Another thing that is very obvious in the above pictures are the lateral cracks that are radiating outward from the crushed zone. The depth to which those cracks occur and under which angle they emerge is again dependent on the angle of foliation and the rock type. Those lateral cracks in connection with radial cracks form the large wedge shaped fragments that are missing from the rock cores in the the above photographs. Another way for chips to develop is that lateral cracks, whether shallow or deep intersect the top core surface.

Figure 51 shows a distinct developed crack pattern and a definite secondary crushed zone of a brittle rock. The crack system spreading from the SCZ consists of four lateral cracks and three deep median cracks. There are just two vent fissures visible in the picture, because the third is in the plane where the core was split.

Figure 51: Crack pattern after a PPT

Figure 52: "Unwrapped", marked and split samples

2.3 Punch Penetration Tests in TBM Performance Prediction

2.3.1 Development of a “PPT model” out of the CSM model

One of the aims of this thesis is to proof that it is possible to improve the accuracy of existing performance prediction models by using Punch Penetration Tests as the main input parameter instead of Uniaxial Compressive Strength and the Brazilian Tensile Strength Tests.

The easiest way to proof this is to replace the UCS and BTS terms ($\sqrt[3]{\sigma_c^2 * \sigma_t}$) in the existing CSM model by the specific penetration for the point of first failure of the PPT. The CSM model is used as a tool here because it provides the possibility to normalize the different geometric parameters R, T, S and p of the different cutting tests.

The existing CSM model calculates the normal force F_N under a disc cutter by the following equation:

$$F_N = 2{,}12 * \sqrt[3]{\frac{\sigma_c^2 * \sigma_t * S}{\varphi * \sqrt{R * T}}} * \varphi * \frac{R}{1000} * \frac{T}{1000} * cos\frac{\varphi}{2}$$

This equation is obtained by rearranging and combining the equations given in 1.3.2.

The improved PPT model calculates the normal force F_N by this equation:

$$\boldsymbol{F_N = 2{,}12 * \sqrt[3]{\frac{S}{\varphi * \sqrt{R * T}}} * \varphi * \frac{R}{1000} * \frac{T}{1000} * cos\frac{\varphi}{2} * \left(a * PPT^b\right)}$$

Uniaxial Compressive Strength UCS	σ_c	MPa
Brazilian Tensile Strength BTS	σ_t	MPa
Cutter radius	R	mm/m
Spacing	S	mm
Disc tip width	T	mm/m
Penetration	p	mm
Angle of the contact area	φ	rad

Averaging stress in the contact area	P^*	MPa
Cutting force	F	kN
Specific penetration of the PPT at First Failure	PPT	kN/mm
Constant	a	-
Exponent	b	-

The normal force F_N and not the total F_T, rolling F_R or side force F_S is used in this model, because it is the only force that is available for all cutting tests and plays, because of its magnitude compared to the other forces, by far the most important role in performance prediction.

2.3.2 Development of a power function to utilize the results of the PPT

To really improve the existing model it is necessary to find a power function like $a * PPT^b$ with the result of the PPT as a part of it, to replace the term $\sqrt[3]{\sigma_c^2 * \sigma_t}$. This power function is found using regression analysis for the PPT results and the associated normalized measured normal force obtained from the linear cutting tests.

The normalization factor for the normal force F_N reads $2{,}12 * \sqrt[3]{\frac{S*\varphi^2}{\sqrt{R*T}}} * \frac{R}{1000} * \frac{T}{1000} * cos\frac{\varphi}{2}$.

It is obtained by following these steps:

The first step is to move the term $\sqrt[3]{\sigma_c^2 * \sigma_t}$ from the right to the left side in the following equation:

$$P^* = 2{,}12 * \sqrt[3]{\frac{\sigma_c^2 * \sigma_t * S}{\varphi * \sqrt{R*T}}} \quad \rightarrow \quad \frac{P^*}{\sqrt[3]{\sigma_c^2 * \sigma_t}} = 2{,}12 * \sqrt[3]{\frac{S}{\varphi * \sqrt{R*T}}}$$

Then P^* is substituted by $2{,}12 * \sqrt[3]{\frac{S}{\varphi * \sqrt{R*T}}}$ in the following equation:

$$F_N = P^* * R * T * \varphi * cos\frac{\varphi}{2} \quad \rightarrow \quad N_{Factor} = 2{,}12 * \sqrt[3]{\frac{S}{\varphi * \sqrt{R*T}}} * R * T * \varphi * cos\frac{\varphi}{2}$$

This normalization factor N_{Factor} is needed for normalizing all the measured normal forces F_N in the LCM tests, which show different values for R, T, S and p, to make them comparable within one diagram.

The normalized measured normal force $F_{N\text{-}Norm}$, which is on the y-axis in the diagram, is finally calculated and plotted against the first failure specific penetration of the PPT (PPT FF SP) for each lithology (except Imberg Sandstone), direction and penetration:

$$F_{N-Norm} = \frac{F_N}{2{,}12 * \sqrt[3]{\frac{S}{\varphi * \sqrt{R * T}}} * R * T * \varphi * cos\frac{\varphi}{2}}$$

The cutting tests of the Imberg Sandstone are not used for the regression analysis, because they show big anomalies caused by some systematic errors during testing which could lead to a distortion of the power function.

Figure 53**Fehler! Verweisquelle konnte nicht gefunden werden.** shows the result of the regression analysis with the following power function:

$$\boldsymbol{y = 26{,}883 * x^{0{,}1149}} \quad \rightarrow \quad \boldsymbol{a = 26{,}883 \; and \; b = 0{,}1149}$$

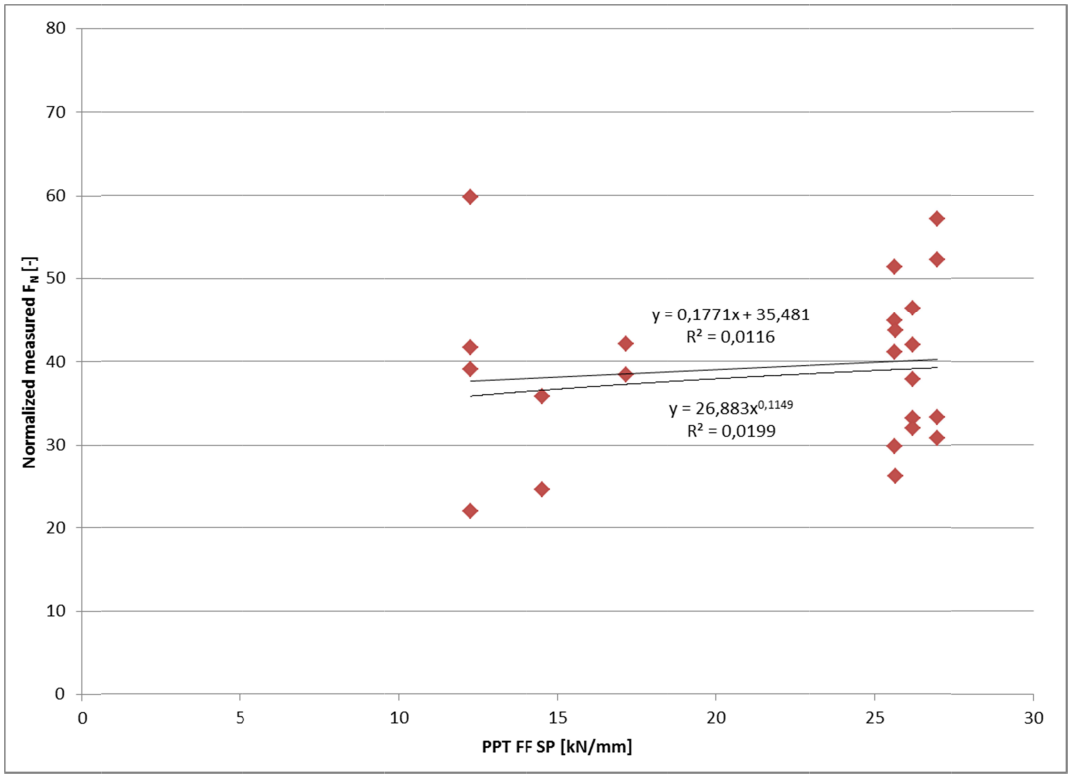

Figure 53: Determination of the power function for the new model

2.3.3 Comparison of the results from the CSM model and the new “PPT model”

The aim of this part is to prove that PPT model with PPT FF SP values provides better results for the cutting force prediction than the existing CSM model with the UCS and BTS values as rock strength input parameters.

Table 11 shows the calculation of the normal forces for the PPT and the CSM model according to the developed formulas in 2.3.1 and a comparison of the obtained results with the actually measured forces.

To make it clearer the predicted normal force out of the PPT is calculated in three steps:

$$F_N = X * Y$$

$$X = a * PPT^b$$

$$Y = 2{,}12 * \sqrt[3]{\frac{S}{\varphi * \sqrt{R * T}}} * \varphi * \frac{R}{1000} * \frac{T}{1000} * cos\frac{\varphi}{2}$$

A comparison of the accuracy of the two models is provided by the four right columns which calculate the standard deviation for each model from the measured forces. At the bottom of the table are two calculated standard deviations. It is 25,70 kN for the PPT model and 71,96 kN for the CSM model. It shows that the new model based on PPT is more accurate than the original CSM model which is based on UCS and BTS.

		PPT model					CSM model	Measured	PPT - Measured		CSM - Measured	
		Penetration	PPT FF SP	Phi	X	Y	FN	FN	PPT-Meas.	(PPT-Meas.)^2	CSM-Meas.	(CSM-Meas.)^2
		[mm]	[kN/mm]	[rad]			[kN]	[kN]				
Augen Gneiss	Normal	5,08	25,65	0,22	39,03	0,00263	**102,75**	**221,66**	**108,20**	-5,45	29,74	113,46	12872,76
		7,62	25,65	0,27	39,03	0,00301	**117,35**	**253,15**	**154,66**	-37,32	1392,63	98,49	9699,55
	Parallel	5,08	25,65	0,22	39,03	0,00263	**102,75**	**221,66**	**78,49**	24,26	588,46	143,17	20497,70
		7,62	25,65	0,27	39,03	0,00301	**117,35**	**253,15**	**135,04**	-17,69	313,09	118,11	13949,98
	Oblique	5,08	25,65	0,22	39,03	0,00263	**102,75**	**221,66**	**68,97**	33,79	1141,46	152,69	23315,36
		7,62	25,65	0,27	39,03	0,00301	**117,35**	**253,15**	**131,37**	-14,02	196,46	121,78	14831,24
Calcareous Mica Schist	Normal	5,08	12,27	0,22	35,86	0,00263	**94,40**	**103,22**	**109,64**	-15,24	232,15	-6,42	41,18
		7,62	12,27	0,27	35,86	0,00301	**107,81**	**117,89**	**179,75**	-71,93	5174,33	-61,86	3826,76
	Parallel	5,08	12,27	0,22	35,86	0,00263	**94,40**	**103,22**	**57,78**	36,62	1341,27	45,44	2065,02
		7,62	12,27	0,27	35,86	0,00301	**107,81**	**117,89**	**117,37**	-9,56	91,40	0,51	0,26
	Oblique	5,08	14,52	0,22	36,56	0,00263	**96,25**	**103,22**	**64,61**	31,64	1000,95	38,61	1490,85
		7,62	14,52	0,27	36,56	0,00301	**109,92**	**117,89**	**107,54**	2,38	5,67	10,35	107,04
Granite Gneiss	Normal	5,00	26,97	0,28	39,25	0,00166	**65,26**	**93,77**	**95,05**	-29,79	887,52	-1,28	1,63
		7,00	26,97	0,33	39,25	0,00185	**72,78**	**104,58**	**96,94**	-24,16	583,69	7,64	58,35
	Parallel	5,00	26,97	0,28	39,25	0,00166	**65,26**	**93,77**	**55,43**	9,83	96,64	38,34	1470,28
		7,00	26,97	0,33	39,25	0,00185	**72,78**	**104,58**	**57,12**	15,66	245,24	47,46	2252,29
Brixen Granite	Oblique	1,27	26,20	0,11	39,12	0,00183	**71,67**	**98,49**	**60,79**	10,88	118,34	37,70	1421,40
		2,54	26,20	0,15	39,12	0,00231	**90,19**	**123,95**	**73,80**	16,39	268,53	50,14	2514,32
		3,81	26,20	0,19	39,12	0,00264	**103,12**	**141,72**	**99,97**	3,15	9,95	41,75	1743,16
		5,08	26,20	0,22	39,12	0,00290	**113,37**	**155,80**	**121,56**	-8,20	67,17	34,24	1172,13
		6,35	26,20	0,24	39,12	0,00312	**121,98**	**167,64**	**144,86**	-22,88	523,52	22,77	518,69
Schist Gneiss	Oblique	5,08	17,16	0,22	37,27	0,00263	**98,11**	**110,03**	**101,19**	-3,07	9,45	8,85	78,25
		7,62	17,16	0,27	37,27	0,00301	**112,05**	**125,66**	**126,54**	-14,49	209,93	-0,88	0,77

Standard Deviation:		**25,70**		**71,96**

Table 11: Comparison of the measured normal forces with the normal forces predicted by the CSM and PPT models

The same observation can be made when examining Figure 54. It is obvious that the dark blue lines representing the PPT model results are in most cases closer to the actual measured forces (represented by the green, violet and light blue lines) than the red lines representing the CSM model.

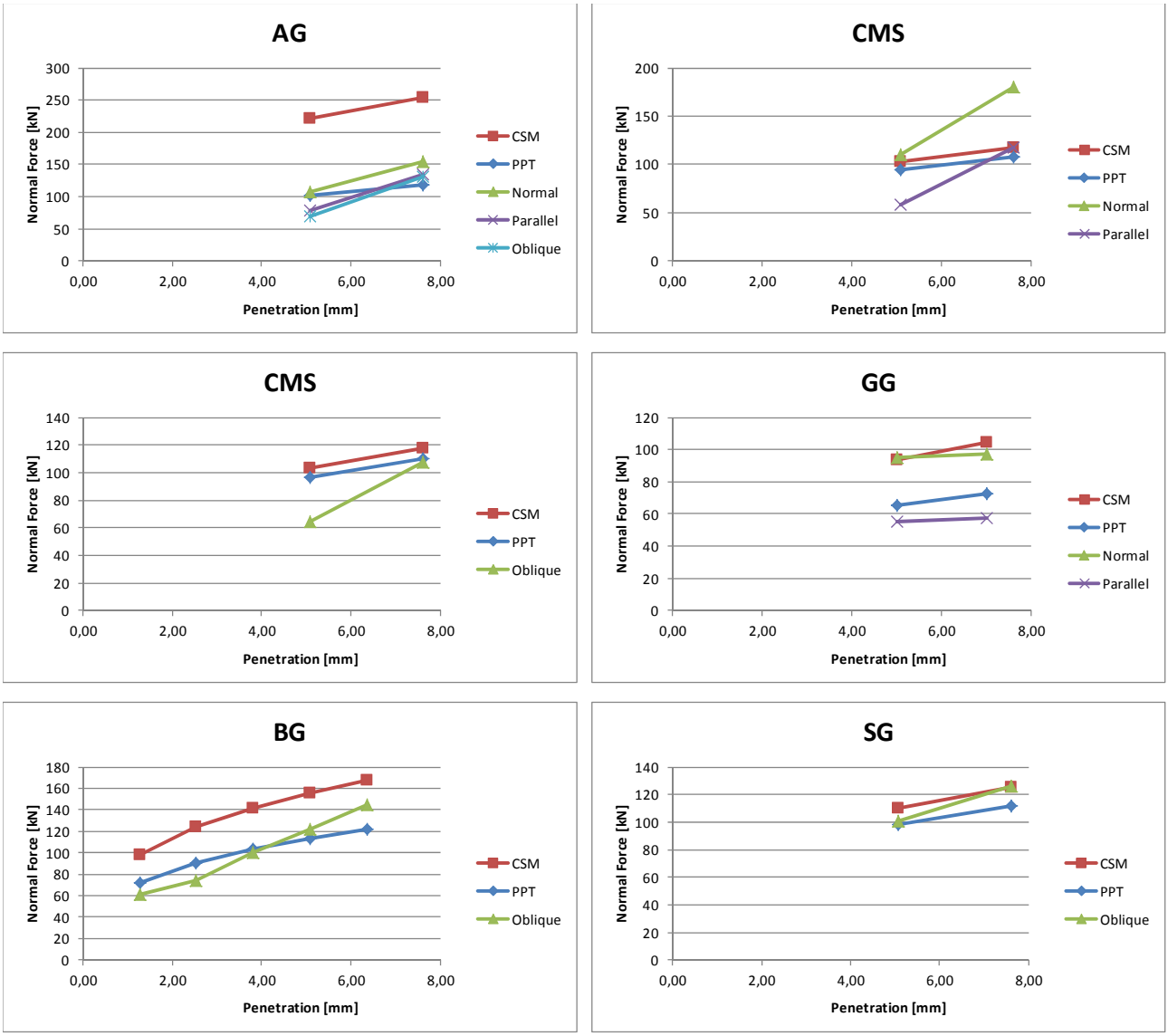

Figure 54: Comparison of the PPT and the CSM model with measured normal forces

Figure 55 is a powerful illustration to see which of the two models is actually better for predicting cutting forces. The closer the colorful lines are to the thick black line, representing a ratio of 1 of the calculated to the measured forces, the closer the calculated forces are to the measured.

Especially for the Augen Gneiss and the Brixen Granite the CSM model fails to predict appropriate forces by generally overestimating them.

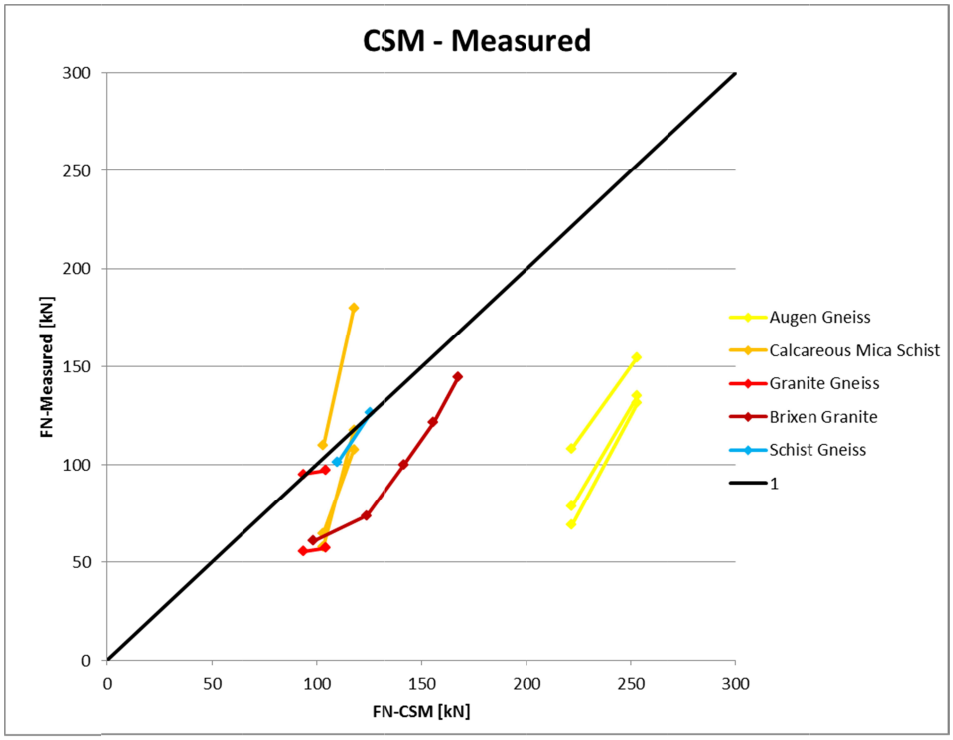

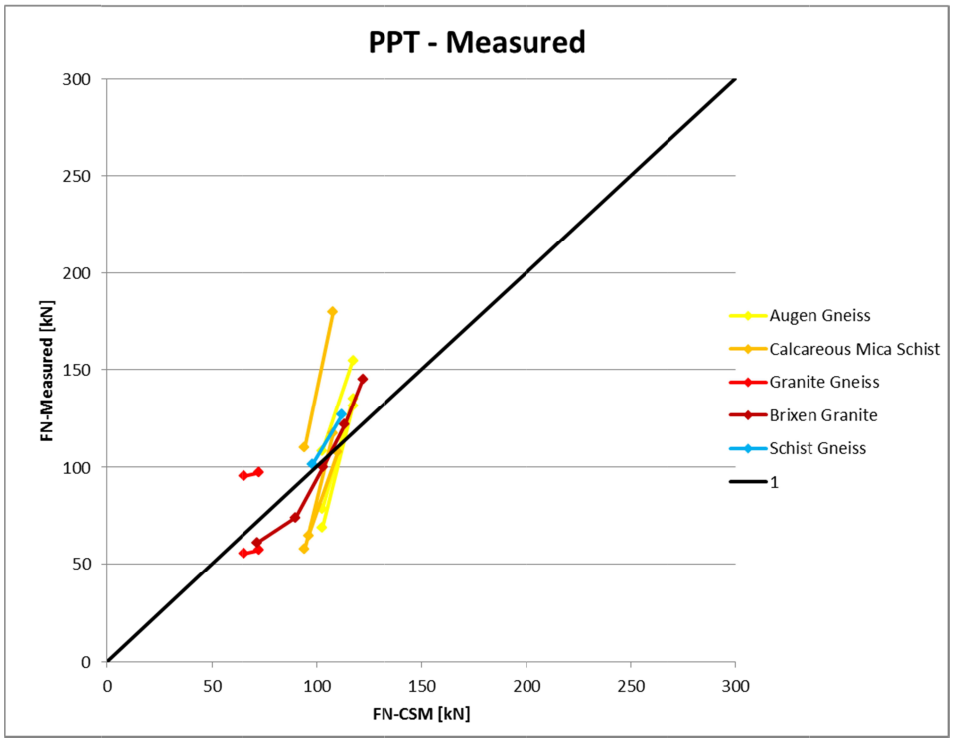

Figure 55: Illustration of the possibility of the different models to predict cutting forces (1)

In Figure 56 on the next page a linear regression is done between all points and the slope of the line is a great value for quantifying the quality of the prediction. The closer the gradient of the line is to 1, the better the prediction is. If the gradient of the regression line is below 1 the model tends to overestimate forces, if it is higher than 1 the model tends to underestimate cutting forces.

For the CSM model the gradient is 0,23 and for the PPT model 1,35. This proofs again that this new PPT model with the specific penetration of the first failure point of the PPT as the main input parameter for rock strength provides better force estimations than the existing CSM model with the UCS and BTS values. In addition the value of 0,23 shows again that the CSM model is by far overestimating cutting forces.

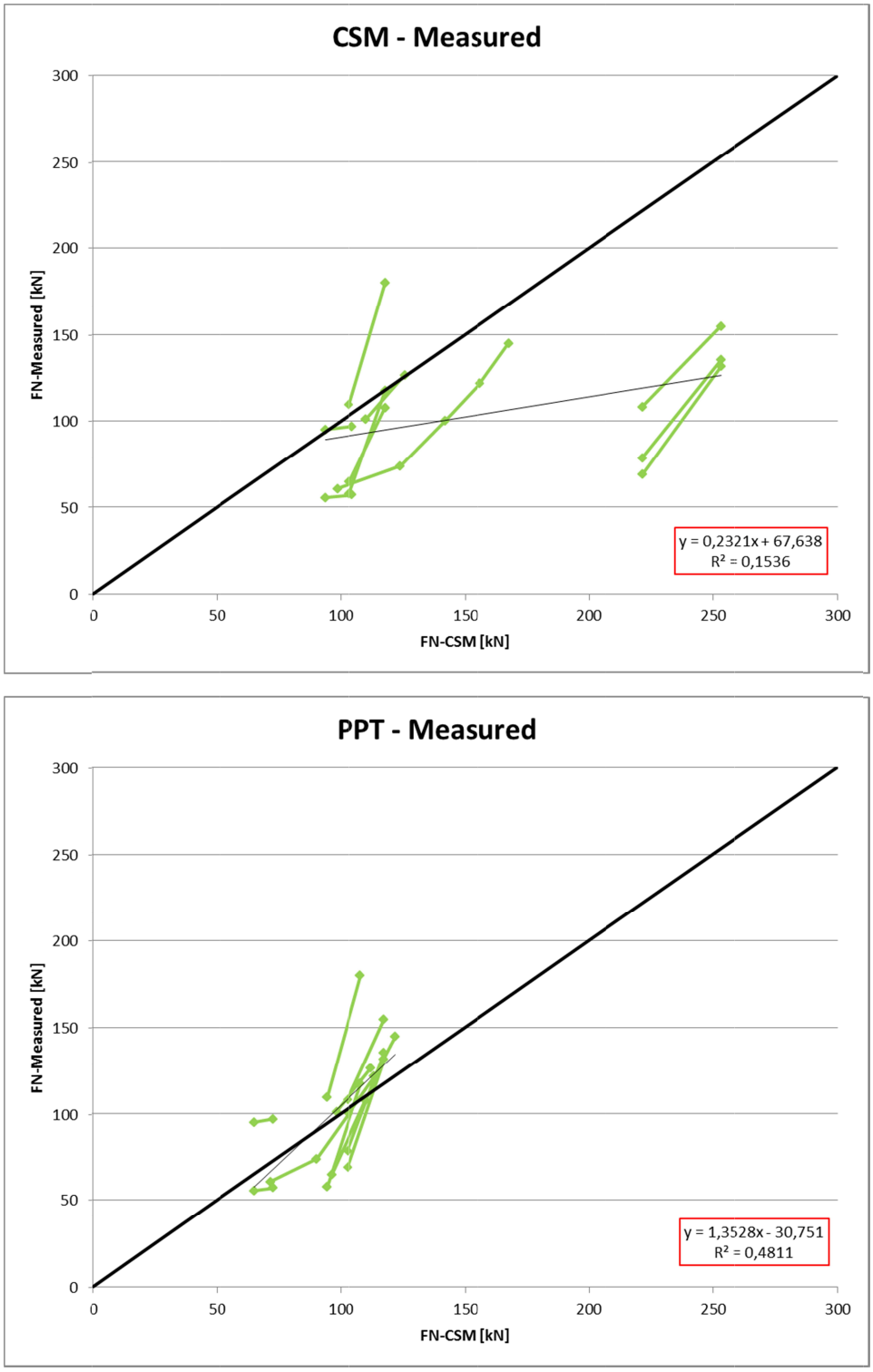

Figure 56: Illustration of the possibility of the different models to predict cutting forces (2)

2.3.4 From cutting forces to performance prediction

Out of the calculated normal force F_N it just takes three more steps to determine the power requirements.

The first thing is to calculate the total force F_T:

$$F_T = \frac{F_N}{cos\frac{\varphi}{2}}$$

Then it is possible to determine the required torque:

$$M = n_c * 0{,}6 * \frac{D_c}{2} * F * sin\frac{\varphi}{2}$$

Finally the power requirement is calculated:

$$P = \frac{\pi}{30} * n * M$$

M	Torque (kNm)
P	Power requirement (MW)
D_C	TBM cutterhead radius (m)
n_C	Number of disc cutters (-)
n	Rotational speed (min^{-1})

The result of the performance prediction model is an estimated rate of penetration (ROP) in millimeter per revolution (mm/rev). This is the excavated distance after one revolution of the cutterhead.

To calculate the ROP it is necessary to go the other way round and estimate the penetration out of the provided power by rearranging the above equations. As soon as the force that the machine is able to transmit to a single disc is determined, one can go into the PPT model equation and express the estimated penetration.

2.3.5 Shortcomings of the “PPT model”

The first and most important thing is that the database for the PPT model is much smaller than the database used for the establishment of the CSM model. Therefore it is a lot easier to find a function which corresponds pretty well with the measured cutting forces especially because the constant *a* and the exponent *b* for the power function are derived from the same lithologies as the comparison is done with.

Another point that needs to be emphasized is that PPT results are better adjusted to cutting tests than UCS and BTS results because loading direction of the PPT and the LCM tests to the foliation of the rock was the same. This is definitely an advantage in this study over the CSM Model which just uses UCS and BTS input parameters that were not measured in accordance to any special direction of the foliation or bedding of planes.

As the PPT model seems to predict cutting forces really well, it is necessary to emphasize the efforts for establishing a large database on which the determination of the factors a and b is based. This database should provide cutting forces from linear cutting tests and specific penetrations at the point of first failure obtained from Punch Penetration Tests. Of course it is necessary to carefully consider and record the orientation of the foliation to the loading direction, because this certainly has an influence.

3. Bibliography

[1] Hucka, V., Das, B. (1974) “Brittleness Determination of Rocks by Different Methods” *Int. J. Rock Mech. Min. Sci. & Geomech. Abstr.* Vol. 11, pp. 389 – 392

[2] Hetényi, M. (1960) “Handbook of experimental stress analysis” *Wiley,* p. 15.

[3] Bieniawski, Z.T. (1967) “Mechanism of brittle fracture of rock” *Int. J. Rock Mech. Min. Sci.* Vol. 4, pp. 395-406

[4] Altindag, R. (2003) “Correlation of specific energy with rock brittleness concepts on rock cutting” *The Journal of the South African Institute of Mining and Metallurgy*, p. 164

[5] Yagiz, S. (2009) “Assessment of brittleness using rock strength and density with punch penetration tests” *Tunneling and Underground Space Technology 24,* pp. 66-74

[6] Dollinger, G.L., Handewith, H.J., Breeds, C.D. (1998) “Use of the Punch Test for Estimating TBM Performance” *Tunneling and Underground Space Technolgy*. Vol. 13, No. 4, pp. 403-408

[7] Gertsch, R.E. (2000) “Rock Toughness and Disc Cutting” *Dissertation,* University of Missouri-Rolla, USA

[8] Lindqvist, P.-A., Lai, H.H. “Behaviour of the Crushed Zone in Rock Indentation” *Rock Mechanics and Engineering 16*, pp. 199-207

[9] Lindqvist, P.-A., Suarez del Rio, L.M., Montoto, M., Tan, X., Kou, S., (1994) “Rock indentation database-testing procedures, results and main conclusions.” *SKB Project Report*

[10] Lindqvist, P.-A., Lai, H.H., Alm, O. (1984) “Indentation Fracture Development in Rock Continously Observed with a Scanning Electron Microscope” *Int. J. Rock Mech. Min. Sci. & Geomech. Abstr.* Vol. 21, No. 4, pp. 165-182

[11] Lindqvist, P.-A., Liu, H.Y., Lou, S.Q., Tang, C.A. (2002) “Numerical simulation of the rock fragmentation process induced by indenters” *International Journal of Rock Mechanics & Mining Sciences.* Vol. 39, pp. 491-505

[12] Leitner, W., Schneider, E. (2005) “Operational Modelling of Advance Rates for Tunnel Boring Machines” *Felsbau 23*. Nr. 6

[13] Yagiz, S. (2002) “Development of rock fracture and brittleness indices to quantify the effects of rock mass features and toughness in the CSM model basic

penetration for hard rock tunneling machines" *Dissertation,* Department of Mining Engineering, Colorado School of Mines, Golden, USA

[14] Frenzel, C., "Leistungs- und Verschleissprognose in der Praxis am Beispiel des CSM-Modells" Department of Mining Engineering, Colorado School of Mines, Golden, USA

[15] NTH-Anleggsdrift & NTH Geologi (1976) "Project Report 1-76 Hard Rock Tunnel Boring" NTNU Trondheim, Norway

[16] Bruland, A. (1998) "Hard Rock Tunnel Boring" *Dissertation,* NTNU Trondheim, Norway

[17] Wikipedia, http://en.wikipedia.org/wiki/Augen, 17.9.2012

[18] Lassnig, K. (2012) "Verwendung von Tunnelausbruchmaterial – Geologische und Geotechnische Aspekte" *Dissertation*, Department Angewandte Geowissenschaften und Geophysik, Montanuniversität Leoben, Austria

[19] Wikipedia, http://en.wikipedia.org/wiki/Granite, 17.9.2012

[20] Bergmeister, K. (2011) "Brenner Base Tunnel: Project status" *Tunnel 2*

[21] Brandner, R., Reiter, F., Töchterle, A. (2008) "Überblick zu den Ergebnissen der geologischen Vorerkundung für den Brenner-Basistunnel" *Geo. Alp,* Vol. 5, pp. 165-174

[22] http://www.geodienst.de/Ruhr%20sandstone%20_engl.pdf, 14.9.2012

[23] Biermeier, F. (2012) „Bestimmung der Einflüsse von Schneidspurabstand, Penetration und Trennflächengefüge auf das Ausbruchsverhalten von mit einer 10 Zoll Diske am Linearprüfstand geschnittenem Imbergsandstein" *Master thesis,* Department Subsurface Engineering, Montanuniversität Leoben, Austria

[24] http://mining.mines.edu/emi/lab_ucs_new.html, 15.9.2012

[25] *http://mining.mines.edu/emi/lab_lcmtest_new.html, 15.9.2012*

[26] Cigla, M. (2006) "Prediction and Modelling of Disc Cutting Forces for Hard Rock Excavation based on Assessment of Punch Penetration Index for Quantifying Rock Toughness and Resistance to Chipping" *Dissertation*, Department of Mining Engineering, Colorado School of Mines, Golden, USA

4. List of figures

5. List of tables